Climate change fuels the destruction of world’s oldest trees

Authors

Clair Barnes, *Centre for Environmental Policy, Imperial College, London, UK*
Theodore Keeping, *Centre for Environmental Policy, Imperial College, London, UK*
Juan Antonio Rivera, *Instituto Argentino de Nivología, Glaciología y Ciencias Ambientales (IANIGLA), CCT CONICET Mendoza, Argentina*
Natalia Liz Pessacg, *Instituto Patagónico para el Estudio de los Ecosistemas Continentales, IPEEC-CONICET, Puerto Madryn, Argentina; National University of Patagonia San Juan Bosco (UNPSJB), Argentina.*
René Garreaud, *Department of Geophysics, Universidad de Chile; Center for Climate and Resilience Research (CR2), Santiago, Chile.*
Mariam Zachariah, *Centre for Environmental Policy, Imperial College, London, UK*
Ben Clarke, *Centre for Environmental Policy, Imperial College, London, UK*
Maisa Rojas Corradi, *Ministry of the Environment, Government of Chile, Santiago, Chile*
Aynur Kadhasanoglu, *Red Cross Red Crescent Climate Centre, The Hague, Netherlands (based in Geneva, Switzerland)*
Ana Mejía, *Red Cross Red Crescent Climate Centre, The Hague, Netherlands (based in Quito, Ecuador)*
Mauricio Santos-Vega, *Red Cross Red Crescent Climate Centre, The Hague, Netherlands (based in Bogota, Colombia)*
Maja Vahlberg, *Red Cross Red Crescent Climate Centre, The Hague, The Netherlands*; *Swedish Red Cross, Stockholm, Sweden (based in Ubmeje/Umeå, Sweden)*
Sneha Ganguly, *Red Cross Red Crescent Climate Centre, The Hague, Netherlands (based in Germany)*
Juan Bazo, *Red Cross Red Crescent Climate Centre, The Hague, Netherlands (based in Sao Paulo, Brazil)*
Friederike Otto, *Centre for Environmental Policy, Imperial College, London, UK*

Review authors

Claire Bergin, *ICARUS Climate Research Centre, Maynooth University, Maynooth, Ireland*
Sjoukje Philip, *Royal Netherlands Meteorological Institute (KNMI), De Bilt, The Netherlands*
Dora Vrkić, *Grantham Institute - Climate Change and the Environment, Imperial College London, London, UK*
Emmanuel Raju, *Department of Public Health, Global Health Section and Copenhagen Centre for Disaster Research, University of Copenhagen*
Virginia Laino, *International Federation of Red Cross and Red Crescent Societies (IFRC), Southern Cone & Brazil Cluster, Buenos Aires, Argentina*

Pablo Bruno, *Argentine Red Cross, Buenos Aires, Argentina*
Tomas Sarkis Badola, *Argentine Red Cross, Buenos Aires, Argentina*
Roop Singh, *Red Cross Red Crescent Climate Centre, The Hague, Netherlands*
Julie Arrighi, *Red Cross Red Crescent Climate Centre, The Hague, Netherlands; American Red Cross, Washington DC, USA*

Cite as Barnes, C. et al., (2026): Climate change fuels the destruction of world's oldest trees (WWA scientific report No. 82) World Weather Attribution DOI: 10.25560/127727

Main findings

- Extreme wildfire danger warnings were issued by national and regional agencies, leading to actions such as strict restrictions on the use of fire and monitoring in Argentina and alerts targeting the general public and authorities in Chile. However, limitations for example in fire monitoring which is dependent on coarse resolution, low frequency fire data, limited budget and changes to the regulation of tourism activities in Argentina may have constrained local capacity to contain the fires quickly.
- In both regions, nonnative needleleaf trees contributed to elevated wildfire risk. Monocultural pine (*pinus radiata*) plantations are highly flammable, due to uninterrupted similar fuel structure, dense tree stands, and species flammability. After past wildfires, fire-adapted pine has replaced native vegetation, as climate continues to increase wildfire risk – the likelihood of succession by fire adapted species and even high wildfire risk increases. Early removal of invasive pines is therefore critical to prevent landscape-scale increases in fire hazard. In Chile, these plantations were adjacent to settlements, as in the case of the similarly devastating Valparaiso fires in 2024. It is therefore key that wildfire risk is strongly accounted for in assessing and regulating current and future land use.
- Wildfires in Patagonia are destroying vast areas of native forest and grassland, putting intense pressure on wildlife found nowhere else. Vulnerable species such as the huemul and the pudú are losing critical habitat, while birds like the Patagonian black woodpecker and many native plants are left without nesting sites or viable seeds. The fires are also encroaching on Los Alerces National Park, a UNESCO World Heritage Site famous for its ancient alerce trees, some of the oldest living trees on Earth.
- To study the different variables leading to high fire danger we compute the hot dry windy index (HDWI) that combines high temperatures, high wind speeds and low humidity. Using this index, we find that the conditions that drove the wildfires in the Chilean and Patagonia regions are characterised as a 1 in 5-year event in today's climate in both regions.
- To assess the role of climate change, we combine observation-based products and climate models and assess changes in the likelihood and intensity of a 1-in-5-year 2-day event over the Chilean region and of a 1-in-5-year 5-day event in Patagonia. In both regions the event would have been rarer in a 1.3C cooler world. In the Chile region events such as this increased in likelihood by a factor of about 3, and a factor of about 2.5 in Patagonia due to human-induced climate change.
- Both regions have experienced very low rainfall in the season preceding the fires that have a return period of 1 in 5 years in today's climate. Combining observation-based data products and climate models we find that fire-season rainfall intensity has decreased by about 25% in

the Chilean region and by about 20% in the Patagonia region. At the same time, temperatures were very high, leading to high evapotranspiration and thus dry vegetation.

- Across both regions, all climate models project a continued shift toward more severe fire weather conditions alongside declining seasonal rainfall. This strong agreement among models gives us high confidence that the changes already observed are driven by climate change.
- In addition to human-induced climate change modes of natural climate variability acting on multiple timescales during the fire season, such as La Niña and the Southern Annular Mode, promoted anticyclonic circulation anomalies that favoured the hot and dry conditions that enhanced fire persistence and severity in parts of the region.
- Ongoing wildfire risk in this region has prompted significant investment into wildfire risk management, including an operational fire risk forecasting system and an "early action protocol" by the Chilean Red Cross to anticipate wildfires based on forecasts, activating action to mitigate the potential impacts of the wildfires in the Araucanía region, including damage to houses, people being exposed to the fires, and risks associated with delayed evacuations.
- Over the last 4 years Chile has increased the budget for combating fires by 110%. These funds have been allocated to forecasting systems, equipment and fire brigades. The impacts of the January fires reinforce the need for effective spatial planning and management of tree plantations, especially at the urban-rural interface. Before new suburban development, it is key that wildfire risk is assessed for. Where existing structures exist in high risk areas, home hardening and vegetation management schemes can substantially reduce risk.

1 Introduction

On the afternoon of 17 January 2026, multiple wildfires ignited in south-central Chile across the Ñuble, Biobio, and Araucanía regions (Figure 1.1). The fires near Concepción city were caused by three nearby ignition points that merged into one single fire, referred to as the Penco-Lirquen fire (centered at 36.7°S, 73°W), which remained active for approximately 36-48 hours. Driven by strong south-southwesterly winds, the fire propagated rapidly downslope towards the coastal settlements of Penco-Lirquen and Punta Parra. There, the fire caused 23 fatalities, destroyed thousands of houses, and damaged critical infrastructure. The fire burned approximately 20,000 hectares in a landscape mostly dominated by non-native forest plantations such as *Pinus radiata* and *Eucalyptus* species.

Central Chile has a Mediterranean climate – featuring a long, warm, and dry summer season. Chillán city, located in the inland valley, had maximum temperatures (Tx) exceeding 30°C almost every day since December 2025, and reached 35°C in two heatwave events before the beginning of the fires. Concepción city, located at the coast, has lower maximum temperatures because of the maritime air influence. The maximum temperatures in the afternoon of 17 January 2026 (just before the fire onset) were 31.5°C in Chillán and 24.5°C in Concepción. Both values were above the average Tx for January-February (29.6°C in Chillán, 22.6°C in Concepción) but not extreme and well below the corresponding daily records since 1970. During January 18th the temperature rose to 37.2°C in Chillán (Dirección Meteorológica de Chile, 2026a), above the 99th percentile threshold, a factor that complicated the firefighting efforts. In Concepción, the temperature remained similar, in part because the thick smoke plume much reduced the solar radiation at the surface. Nevertheless, Tx reached 26.3°C, a value that exceeds the 90th percentile of summer days.

The January 2026 Penco-Lirquen event adds to the increasingly extreme record of major forest fires in Chile over the last decade (Gonzalez et al. 2018). These include the Viña del Mar event in February 2024, which caused 138 fatalities (WWA, 2024), and the megafires in central Chile in January 2017 and February 2023 that burned more than 500 thousand hectares each, about 10 times the historical mean, country-wide fire damage (Carrasco-Escaff et al. 2024). The Penco-Lirquen event is akin to the Viña del Mar event as a rapidly spreading downslope wildfire that spread through planted vegetation into urban areas.

The event developed under a strong upper-level ridge and the growing phase of a coastal low that resulted in warm, dry, and windy conditions (Garreaud et al., 2002). In between the high pressure system and the coastal low, there are easterly (offshore) winds in the lower troposphere that, among other things, lead to the Puelche winds (Montecinos et al., 2017) on the western slope of the Andes. This forced subsidence brings warm and dry air to the lower free troposphere over the central valley and coastal regions that can be entrained into the boundary layer during the day. Thus, the synoptic and sub-synoptic environment of 17-18 January 2026 was similar to the patterns previously identified during major fires in south central Chile (Carrasco-Escaff et al., 2024).

The wildfire was controlled after 2 days of intense work by firefighters from local municipalities, the national forest service (CONAF) and private companies. Meteorological conditions also played a significant role in fire suppression, as the end of the coastal low on 19 January 2026 led to the re-establishment of the marine boundary layer, with low clouds advancing from north to south. In this stage, there was also onshore flow that transported the smoke inland, causing bad air quality in several sites.

In the North Patagonian Andes of Argentina, 2026 began with anomalously high temperatures and prolonged drought conditions, with the last significant rainfall recorded in mid-November 2025. Heatwave conditions (at least three consecutive days with Tx and minimum temperatures (Tn) above the 90th percentile) were observed during the first week of January across central-western Argentine Patagonia (40°S-43°S), affecting Bariloche, El Bolsón and Esquel cities (SMN, 2026a). Notably, El Bolsón station recorded its highest January temperature on record (38.4°C on January 5). Esquel station experienced a second heatwave event from 9 to 11 January and recorded 11 consecutive days of extreme maximum temperatures, representing the second-longest warm spell in the past 65 years. This combination of hot and dry conditions favoured the occurrence and propagation of wildfires around the Los Alerces and Lago Puelo National Parks and in nearby regions (Figure 1.1) in the first week of January, with fires persisting for several days under sustained fire-weather conditions. Although rainfall occurred during 11, 14 and 27 January, the accumulation ranged from 2 to 3 mm, amounts insufficient to suppress the fires, which remained active into the first week of February, even after 5 mm rainfall on 2 February. A third heatwave event occurred between late January and early February (SMN, 2026b), a situation observed only three times in the last 65 years in Esquel temperature records.

The wildfires that affected the northern Patagonian Andes during the summer of 2026 have caused unprecedented environmental, social, and economic consequences for the region. The first fires officially began on January 5 in the Puerto Patriada area—at the height of the tourist season, with more than three thousand visitors present—and spread rapidly on January 6, burning 1,800 hectares in a single day and forcing the complete evacuation of the village. In Chubut Province, where wildfires are the leading cause of deforestation (Mónaco et al., 2019), the government confirmed that the fire had been intentionally set. By the first week of February, multiple active fire fronts were still affecting the region, with estimates of more than 45,000 hectares of native and planted forest, shrublands, and grasslands burned, including the estimated loss of 75% of Epuyén's native forests. The impact on local communities was equally severe, with numerous losses of homes and livestock. Wildfires burned more than 106,000 ha in Chubut between the 2014/15 and 2024/25 fire seasons, with the last 5 seasons recording 436 fire outbreaks and 37,750 ha affected, including interface fires that resulted in infrastructure losses. Prolonged droughts, strong winds, accumulated fuel loads, and human activities—36% of fires linked to burning practices and 25% attributed to intentional ignition—have all contributed to elevated fire risk across Andean-Patagonian forests and transitional areas toward the steppe. Native forest was the most affected vegetation type (47%), followed by shrublands and grasslands, with consequent impacts on wildlife, soils, and water resources (Secretaría de Bosques, 2025). Within this long-standing context of high fire occurrence and ecosystem vulnerability, the 2026 wildfire stands out as one of the most significant and damaging events in the region.

Circulation anomalies during January 2026 indicate the persistence of a mid-level ridge and a low-level anticyclone over much of southern South America, particularly south of 40°S, a pattern that is characteristic of the occurrence of heatwaves over Patagonia (Jacques-Coper et al., 2016). This configuration can be linked to a persistent and active phase 6 of the Madden-Julian Oscillation (MJO) in the beginning of January, transitioning to an active phase 7 after January 22, a mechanism previously highlighted as a precursor of warm anomalies over central Chile and the North Patagonian Andes of Argentina (Alvarez et al., 2016; Jacques-Coper et al., 2021). The prevailing anticyclonic circulation over southern South America inhibits precipitation in the region and promotes negative soil moisture anomalies (Collazo et al., 2024), factors that favoured the persistence and propagation of the fires. Prevalent La Niña conditions during Southern Hemisphere Summer (CPC, 2026a) and a persistent positive phase of the Southern Annular Mode (SAM) observed since January 7 (CPC, 2026b) are also drivers for the enhanced anticyclonic circulation in mid-latitudes leading to warm temperatures and dry conditions, factors previously identified with the occurrence of large fires in Patagonia (Veblen et al., 2011).

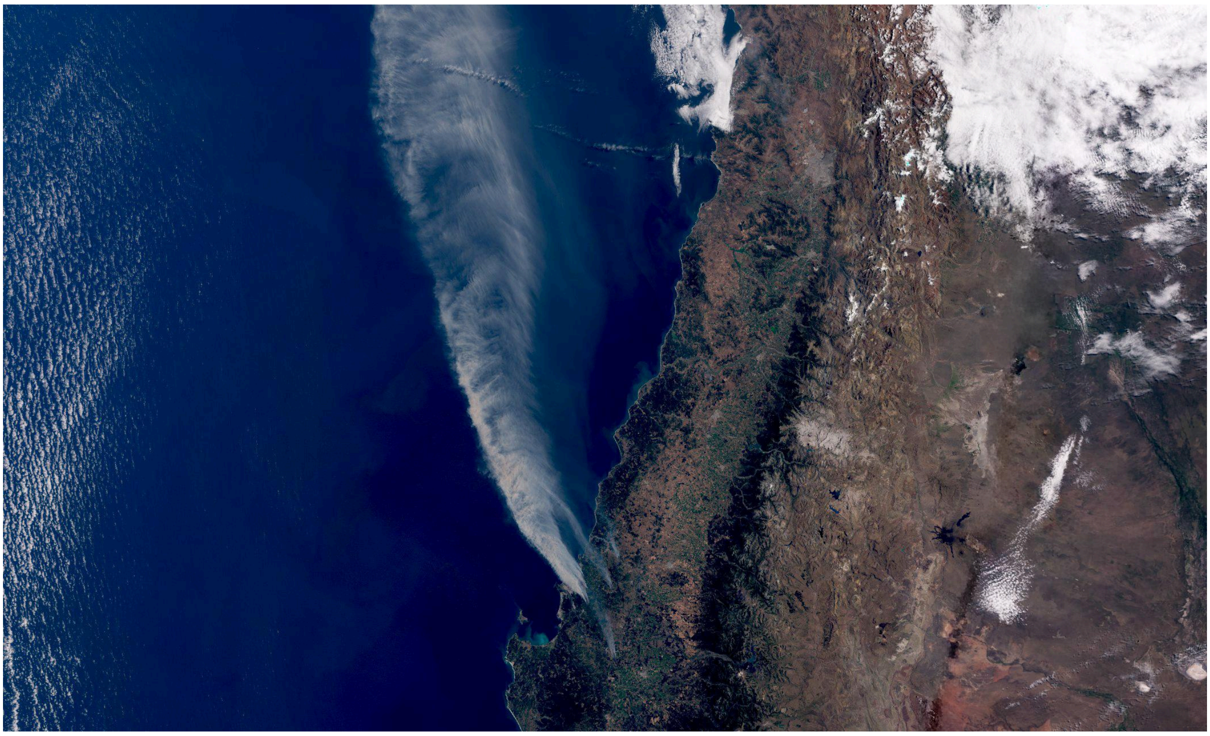

Figure 1.1:. EUMETSAT images showing the occurrences of fires in Chile during January 18 (EUMETSAT, 2026).

These fires were developed following a dry winter in central Chile (Dirección Meteorológica de Chile, 2026b) and the North Patagonian Andes of Argentina (SMN, 2025), within a broader context of persistent drought conditions over the past 15 years (Garreaud et al., 2020). In addition, warming trends have been observed in both regions (Brendel et al., 2020; Piticar, 2019), particularly off the Chilean coast (Falvey and Garreaud, 2009), along with increases in the frequency of temperature extremes and in heatwave characteristics such as duration and intensity (González-Reyes et al., 2023; Cimolai and Aguilar, 2024). This combination of increasingly hot and dry conditions has contributed to an increase in the number of fires over the last 4 decades (Urrutia-Jalabert et al., 2018; Barberá et al., 2025), although increasing lightning activity also resulted in higher fire ignition (Kitzberger and Bürgesser, 2025). Under a middle-of-the-road emissions scenario, there is high confidence in projected increases in fire-weather conditions over southwestern South America by mid-century, with medium confidence for southern South America (Ranasinghe et al., 2021). This underscores the increasing wildfire risks in a context of regional warming and long-term drying trends associated with anthropogenic forcing.

1.1 Event Definition

For the event definition (both spatial and temporal) two things are important: the relation to the impact of the event, and the climatological homogeneity of the area. We investigate a Hot-Dry-windy index (HDWI) that combines high temperatures, high wind speeds and low humidity to assess a combination of different variables that increase fire risk. HDWI is based on the product of the maximum wind speed and the maximum vapour pressure deficit (VPD) within the lowest 50 millibars of the atmosphere (Srock et al., 2018; HDWI, 2024). VPD has a linear effect on the rate of evapotranspiration, meaning that the maximum fire fuel flammability is strongly affected by the daily maximum VPD. Surface windspeed also has a strong control on moisture transport from fuels, as well as being key to the rate of fire spread. We chose the HDWI as it is a straightforward daily index directly proportional to physical drivers of wildfire severity, and was not developed for a specific context, such as the widely used Canadian Fire Weather Index. Scaling with fuel flammability and likely wildfire spread rate, the HDWI is therefore a useful hazard metric for estimating threat to communities and difficulty of containment. Whilst more complex indices account for long term drying effects on the fuel bed, the HDWI is solely focussed on daily extrema in fire weather conditions. HDWI is expressed as

$$HDW = U \times VPD\ (T,q)$$

where U is wind speed and VPD is vapour pressure deficit (a function of temperature T and relative humidity q).

We focus on two regions, in Chile the most affected region between the coast and the foothills of the Andes around the Ñuble, Biobío and La Araucanía regions [71.5°W - coast; 36-38°S] and a box containing the most affected region across the Chilean and Argentine border in northern Patagonia [41.4 - 43.4°S; 70.6 - 72.6°W] (Figure 1.2). For Chile, we focus on the 2 days of highest HDWI and Patagonia 5-day maximum HDWI from December-February, reflecting the different lengths of peaks wildfire activity associated with the fires in each region.

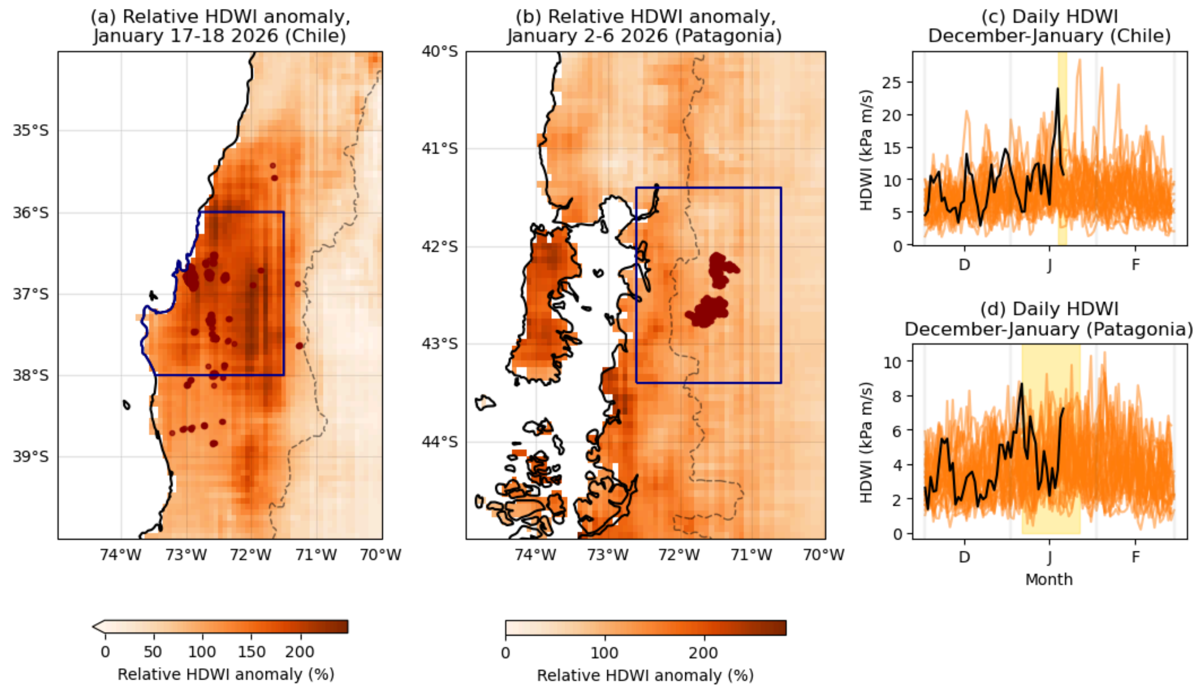

Figure 1.2: (a,b) Maps of relative HDWI anomaly with respect to the 1990-2020 DJF climatology in each region, prior to and during the fire activity: (a) Anomaly of two-day mean HDWI in the Chilean study region; (b) Anomaly of 5-day mean HDWI in the Patagonian study region. Red dots mark active

fires from January 17-19 in Chile and from January 6-20 in Patagonia, according to MODIS data; dark blue outline denotes the study region in each country. (c,d) Time series of daily HDWI averaged over the regions outlined in dark blue in (a,b). Black line represents 2026, while orange lines are years from 2000-2026. Yellow shading indicates the days when the fires were most active (at time of writing). All HDWI data are from ERA5-Land.

To also account for the longer term drying, we additionally analyse precipitation preceding the fire-season, focussing on the same two regions and seasonal precipitation in early summer, November - January (NDJ) (Figure 1.3).

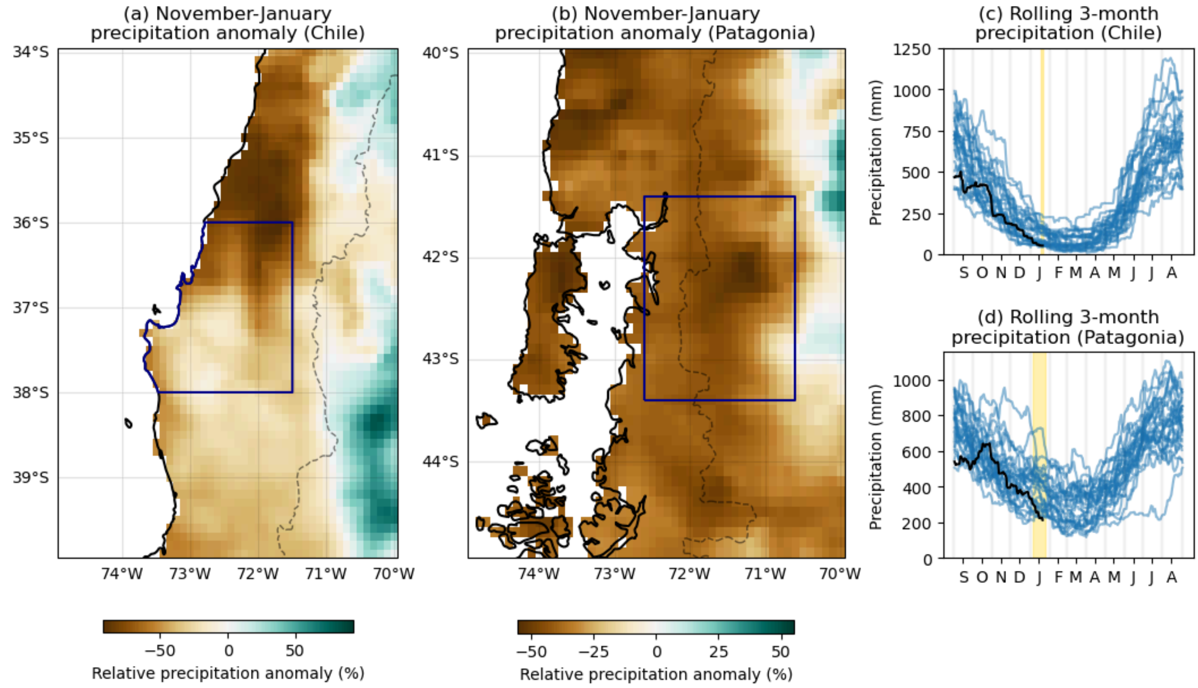

Figure 1.3: (a,b) Maps of relative November-January precipitation anomaly with respect to the 1990-2020 climatology in each region: (a) in the Chilean study region; (b) in the Patagonian study region. Dark blue outline denotes the study region in each country. (c,d) Time series of 91-day running accumulated precipitation over the study regions outlined in dark blue in (a,b). Black line represents 2026, while blue lines are years from 2000-2026. All precipitation data are from ERA5-Land.

In this report, we study the influence of anthropogenic climate change by comparing the likelihood and intensity of similar 2-day and 5-day maximum HDWI events and NDJ precipitation in the present climate with those in a 1.3°C cooler climate, representing the preindustrial past without human-caused warming (1850-1900, based on the Global Warming Index). We also extend this analysis into the future by assessing the influence of a further 1.3°C of global warming from present. This is in line with the latest Emissions Gap Report from the United Nations Environment Programme, which shows that the world is on track for at least 2.6°C temperature rise given currently implemented policies (UNEP, 2024).

2 Observational analysis

2.1 Chile

2.1.1 Trends in HDWI2x

Figure 2.1a shows HDWI2x in the Chilean study region, calculated from the ERA5-Land dataset. Much higher values have been recorded in recent years than previously, and the trend appears to be associated more with a change in the variability of the index than a change in the mean trend. To model HDWI2x we therefore assume not only a linear trend in the mean value that depends on GMST, but also an increase in the variance of the distribution that depends exponentially on GMST (to ensure that the variance remains strictly positive). The fitted model (black line) reflects the trend in mean HDWI, while the blue lines represent the expected magnitude of 1-in-6-year (thick line) and 1-in-40-year (thin line) events. While the mean trend increases only very slightly with GMST, the expected HDWI for more unusual events has increased rapidly, approximately in line with the nonparametric trend (green dashed line). Panel b shows return level curves for the expected magnitude of HDWI2x in the 2026 climate (red line) and a 1.3°C cooler climate without human-caused warming The points representing observed values lie close to the line, indicating that the chosen model captures the distribution of the data well.

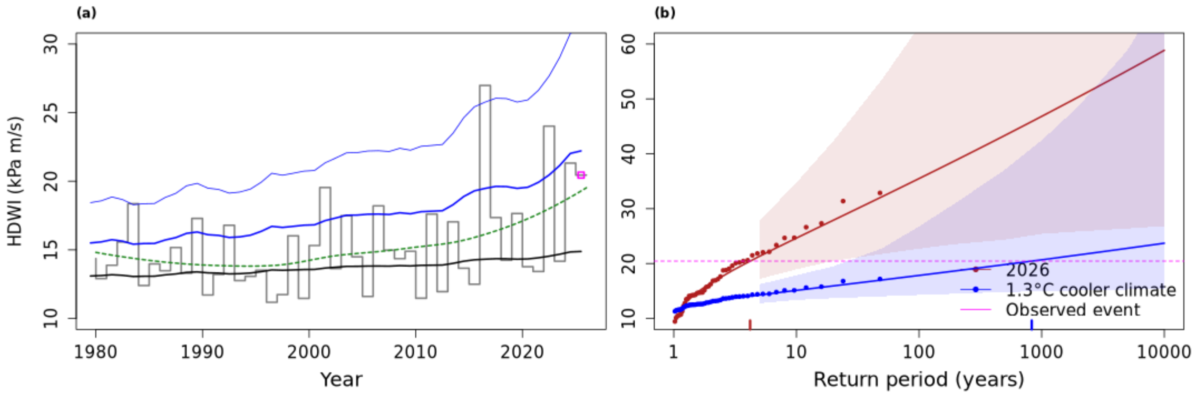

*Figure 2.1: **(a)** Annual time series of HDWI2x in the Chilean study region, with fitted model (dependent on GMST only) overlaid. Solid black line denotes the expected 2-day peak HDWI each year, given the observed values of the smoothed GMST. Blue lines indicate the expected magnitude each year of a 1-in-6-year (thick line) and 1-in-40-year low rainfall event (thin line). Green dashed line is a nonparametric Loess smoother. 2025-26 value is highlighted with a magenta box. **(b)** Return level plots showing the expected magnitude of events of a given return period in the climate of 2026 (red) and a climate with 1.3ºC cooler climate (blue). Historic observations are shown twice: shifted to the current climate (red points) and shifted to the climate of the pre-industrial era (blue points). Shading regions indicate a bootstrapped 95% confidence interval. The magenta line shows the magnitude of the 2026 peak. All data: ERA5-Land.*

Having identified the form of the statistical model, to identify which modes of variability contribute most to changes in annual maximum 2-day HDWI (HDWI2x) in this region, we first fit a statistical model in which HDWI depends on GMST and different combinations of ENSO and the detrended SAM (see Section A1.3). Estimated changes in HDWI2x are shown in Table 2.1, along with the estimated return period of the 2026 maximum and the AIC, a measure of how well the model fits the data. In all four versions of the model, increased warming is consistently associated with an increase of around 3.5 - 6.4 kPa m/s (20-45%); the current weak La Niña adds a further 1.8-3.2 kPa m/s (10-20%), while the December SAM state is associated with a further of 0.5-0.1.8 (2-10%). The AIC indicates that the model that best fits the data includes only the GMST, although all variants receive similar scores.

The return period of the 2026 peak HDWI5x in the current climate is estimated to be 3-4 years, indicating a relatively commonplace occurrence; however, this has been made substantially more likely by climate change, with similarly extreme values now estimated to be 198 times more likely in the GMST-only model, although the uncertainty about this interval is very wide (95% confidence interval: 2.5 times more likely, infinitely more likely). For the attribution analysis, we use an event with an expected return period of 5 years in the current climate.

Covariates	2026 value (kPa m/s)	Change in HDWI2x (Chile)			AIC
		GMST	ENSO	SAM	
GMST only	20.4	6.39 (2.17, 8.13)	-	-	229
GMST + ENSO		5.25 (-23.1, 8.17)	1.81 (-1.34, 4.98)	-	230
GMST + SAM		6.39 (-4.81, 8.65)	-	0.547 (-2.06, 3.68)	232
GMST + ENSO + SAM		3.53 (-673, 8.97)	3.26 (-1.98, 8.21)	1.86 (-1.55, 5.34)	230

Table 2.1: Change in intensity of HDWI2x in Chile region associated with each factor, estimated using different combinations of relevant covariates. AIC is a measure of how well each model fits the data, penalised by the number of parameters in the model to avoid over-fitting, with lower scores indicating a better fit. The model used in the attribution analysis, which is also the best fit to the data, is highlighted in yellow.

Covariates	Return period	Change in likelihood (Chile)			AIC
		GMST	ENSO	SAM	
GMST only	*4.19 (2.27, 18.5)*	*198 (2.53, Inf)*	-	-	*229*
GMST + ENSO	*4.38 (2.2, 17.2)*	*27.8 (0.317, Inf)*	*1.73 (0.825, 210)*	-	*230*
GMST + SAM	*3.95 (2.11, 20.6)*	*89.1 (0.392, Inf)*	-	*1.12 (0.638, 4.15)*	*232*
GMST + ENSO + SAM	*3.47 (1.76, 12.9)*	*2.31 (0.257, Inf)*	*2.42 (0.779, 151)*	*1.53 (0.728, 8.37)*	*230*

Table 2.2: As Table 2.1, but for the probability ratio (factor change in likelihood of similarly high HDWI2x in this region). The model used in the attribution analysis, which received the lowest AIC score, is highlighted in yellow.

2.1.2 Trends in November-January precipitation

To identify which modes of variability contribute most to changes in NDJ precipitation in Chile, we first fit a statistical model in which the log of the accumulated NDJ rainfall depends linearly on GMST and different combinations of ENSO and the detrended SAM. Estimated changes in the intensity of NDJ rainfall are shown in Table 2.3, along with the estimated return period of NDJ precipitation as low as that observed in 2025-2026 and the AIC, a measure of how well the model fits the data, where a lower AIC means a better fit. In all four versions of the model, increased warming is associated with a strong drying trend of 40-50%, indicating that this trend is robust to the choice of additional covariates. The current weak La Niña state is associated with a further reduction of 15-20%, while we would expect 30-40% more precipitation due to the December 2025 SAM state.

In all variants, the 2025-26 low rainfall is only slightly unusual, with a return period of between 3-8 years, although it is more unusual when the recent SAM state is taken into account. Estimates of the probability ratio (the factor change in the likelihood of a November-January period as dry as 2025-2026) associated with 1.3 degrees of warming vary from 4-23 times as likely, depending on the model, but the uncertainty about all of these estimates is very high (Table A2.1). The AIC indicates that models that include the SAM fit the data much better than models that do not, with the best fit obtained by including both ENSO and SAM. Results for this model are discussed in detail below.

Because of the difficulty of obtaining time series of ENSO and SAM for climate models within the time frame of a rapid study, the full attribution analysis is carried out using a statistical model in which NDJ precipitation depends on GMST only, for an event with a return period of 5 years. Although this is not expected to capture all of the variability in the time series, we expect estimates of the mean GMST-dependent trend to be robust.

Covariates	**% change in NDJ precipitation**			**Return period**	**AIC**
	GMST	**ENSO**	**SAM**		
GMST only	-50.0 (-74.2, 2.14)	-	-	2.8 (1.65, 7.5)	72.8
GMST + ENSO	-41.2 (-70.8, 30)	-21.5 (-35, -6.76)	-	2.53 (1.47, 7.79)	69.4
GMST + SAM	-50 (-74, 8.62)	-	39.8 (18.5, 71.2)	7.29 (2.94, 88.8)	65.2
GMST + ENSO + SAM	-44.1 (-70.9, 25.1)	-15.2 (-30.1, 2.02)	32.9 (10.7, 63)	5.68 (2.46, 60.7)	64.5

Table 2.3: Change in relative intensity of NDJ precipitation in Chile associated with each factor, estimated using different combinations of relevant covariates. AIC is a measure of how well each model fits the data, penalised by the number of parameters in the model to avoid over-fitting, with lower scores indicating a better fit. The model used in the attribution analysis is highlighted in yellow, while the model that fits the data best is shaded purple.

The fitted trend over time, given the values of the three covariates in each year, is shown in Figure 2.2(a). The fitted model (black line) captures the general trend in the data (green dashed line), although there is some additional decadal variability not accounted for by the model, with 2000-2015 somewhat wetter than predicted. Corresponding plots showing the fitted model as a function of each covariate are shown in Figure A2.1. Figure 2.2(b) shows return level curves for the expected magnitude of NDJ precipitation in the 2026 climate (red line) and a 1.3°C cooler climate without human-caused warming (blue line). The points representing observed values lie close to the line and well within the 95% confidence intervals, indicating that the model captures the distribution of the data well.

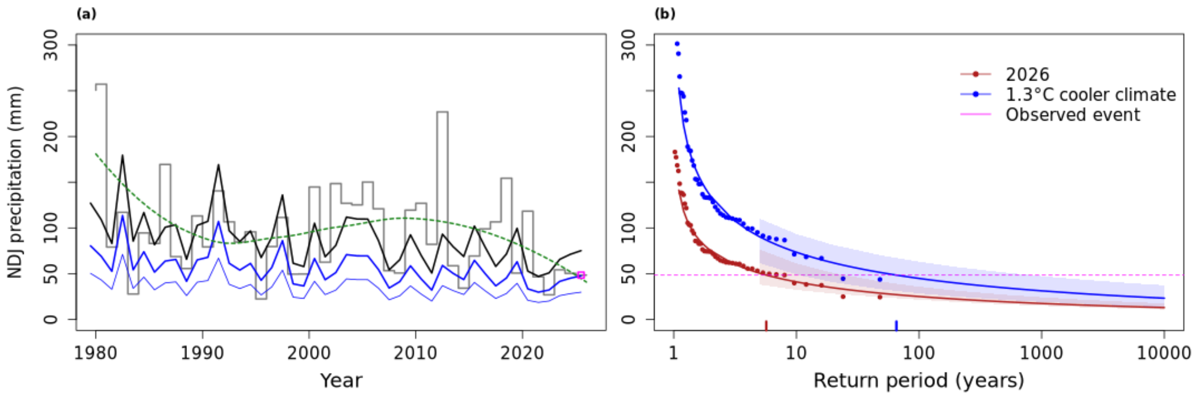

*Figure 2.2: **(a)** Annual time series of NDJ precipitation in Chile, with fitted model overlaid. Solid black line denotes the expected NDJ precipitation each year, given the observed values of the smoothed GMST, Niño3.4 index and December SAM index. Blue lines indicate the expected magnitude each year of a 1-in-6-year (thick line) and 1-in-40-year low rainfall event (thin line). Green dashed line is a nonparametric Loess smoother. 2025-26 value is highlighted with a magenta box. **(b)** Return level plots showing the expected magnitude of events of a given return period in the climate of 2026 (red) and a climate with 1.3°C cooler climate (blue). Historic observations are shown twice: shifted to the current climate (red points) and shifted to the climate of the pre-industrial era (blue points). Shading regions indicate a bootstrapped 95% confidence interval. The magenta line shows the magnitude of the 2025-2026 NDJ rainfall. All data: ERA5-Land.*

2.1.3 Trends in effective precipitation

While there is evidence of a reduction in NDJ precipitation in the Chile study region, fire-prone conditions do not only depend on rain. Effective precipitation (precipitation minus potential evapotranspiration) is the measure of the ideal moisture flux given available surface moisture, with maintained negative values signifying a persistent drying pressure over the landscape. Sustained dry conditions over monthly timescales determine the drying of bulky fuels (Fosberg, 1981). Lengthy drying periods, driven by low precipitation relative to drying, also lead to increased vegetation mortality (McDowell et al., 2022) and reduced rates of decomposition (Cornwell et al., 2009) – increasing dry fuel loads. More abundant, drier fuels substantially increases the likelihood of intense, high mortality wildfire events (MacDonald et al., 2023), such as those seen in Patagonia in January, 2026. We now briefly consider observed trends in potential evapotranspiration (PET) and effective precipitation, although we do not carry out a full attribution.

Potential evapotranspiration (PET) was estimated using the Hargreaves equation (Hargreaves and Samani, 1985; see Section A1.1). The expected changes in NDJ PET are shown in Table A2.2.

Estimated changes in PET due to each factor are consistent across all model variants, with around 6-7% more PET associated with 1.3°C of warming, 2% with the current ENSO state, and around 1% less associated with the December SAM state.

Table 2.4 shows the expected change in daily effective precipitation (in mm) associated with each factor in each of the models. Again we see that the change is fairly robust across all four model variants, with an estimated 0.9-1.1mm (25-33%) less effective precipitation associated with 1.3°C of warming; 0.2-0.3mm (5-7%) less associated with the current weak La Niña state; and 0.3-0.4mm (7-8%) more effective precipitation due to the December SAM state. This result highlights the compounding effect of increasing temperatures in further reducing available water in this region.

Covariates	**NDJ 2026 (mm/day)**	**Change in NDJ effective precipitation (mm)**			**Return period**	**AIC**
		GMST	**ENSO**	**SAM**		
GMST only	-4.53	-1.12 (-1.98, -0.239)	-	-	3.62 (2.07, 11)	103
GMST + ENSO		-0.913 (-1.79, -0.0261)	-0.313 (-0.53, -0.119)	-	3.27 (1.85, 10.1)	99.8
GMST + SAM		-1.12 (-2.03, -0.125)	-	0.396 (0.188, 0.641)	10 (3.73, 256)	97.2
GMST + ENSO + SAM		-0.972 (-1.88, -0.00915)	-0.224 (-0.465, 0.00649)	0.327 (0.093, 0.589)	7.57 (3.01, 147)	96.2

Table 2.4: Change in intensity of NDJ effective precipitation in Chile associated with each factor, estimated using different combinations of relevant covariates. AIC is a measure of how well each model fits the data, penalised by the number of parameters in the model to avoid over-fitting, with lower scores indicating a better fit. The model used in the attribution analysis is highlighted in yellow, while the model discussed in the text is shaded purple.

2.2 Patagonia

2.2.1 Trends in HDWI5x

To identify which modes of variability contribute most to changes in annual (Jul-Jun) maximum 5-day HDWI (HDWI5x) in this region, we first fit a statistical model in which HDWI depends linearly on GMST and different combinations of ENSO and the detrended SAM (see Section A1.3). Estimated changes in HDWI5x are shown in Table 2.5, along with the estimated return period of the 2026 maximum and the AIC, a measure of how well the model fits the data. In all four versions of the model, increased warming is consistently associated with an increase of around 1.8 (an increase of 37%, with uncertainty bounds of 16-67%), indicating that this trend is very robust to the choice of additional covariates. The current weak La Niña state has a very small effect, reducing expected HDWI by up to 2.5%, while the December SAM state is associated with a further reduction of 0.3-0.4 (4-7%). The AIC indicates that the model that best fits the data includes both GMST and SAM as covariates, but the difference in the score is marginal; since the December SAM state did not contribute to the extremeness of the HDWI in 2025-26, we instead consider the GMST-only model, which gives almost the same estimate of the mean trend, but better constrained probability ratios (Table 2.6).

The return period of the 2026 peak HDWI5x in the current climate is around 2-4 years, indicating a relatively ordinary value; however, this has been made at at least an estimated 24 times more likely by climate change, implying that without human-caused warming, similarly high HDWI5x would have been expected at most around once every 46 years. For the attribution analysis, we use an event with an expected return period of 5 years in the current climate.

Covariates	2026 value (kPa m/s)	Change in HDWI5x (Patagonia)			AIC
		GMST	ENSO	SAM	
GMST only	6.58	1.78 (0.947, 2.5)	-	-	110
GMST + ENSO		1.81 (0.94, 2.53)	-0.035 (-0.333, 0.347)	-	112
GMST + SAM		1.77 (0.9, 2.55)	-	-0.304 (-0.66, 0.064)	110
GMST + ENSO + SAM		1.78 (1.02, 2.64)	-0.181 (-0.405, 0.316)	-0.479 (-0.711, 0.0664)	111

Table 2.5: Change in intensity of HDWI5x in Argentinian study region associated with each factor, estimated using different combinations of relevant covariates. AIC is a measure of how well each model fits the data, penalised by the number of parameters in the model to avoid over-fitting, with lower scores indicating a better fit. The model used in the attribution analysis is highlighted in yellow, while the model that fits the data best is shaded purple.

Covariates	Return period	Change in likelihood (Patagonia)	AIC

		GMST	ENSO	SAM	
GMST only	1.92 (1.29, 3.97)	24 (4.77, Inf)	-	-	110
GMST + ENSO	1.93 (1.25, 4.18)	25.9 (4.31, Inf)	0.963 (0.684, 1.46)	-	112
GMST + SAM	2.6 (1.47, 7.11)	1170 (4.79, Inf)	-	0.697 (0.358, 1.07)	110
GMST + ENSO + SAM	3.6 (1.56, 10.4)	Inf (3.94, Inf)	0.74 (0.406, 1.56)	0.516 (0.219, 1.08)	111

Table 2.6: As Table 5, but for the probability ratio (factor change in likelihood of similarly high HDWI5x in this region). The model used in the attribution analysis is highlighted in yellow, while the model that fits the data best is shaded purple.

The fitted trend over time, given the GMST in each year, is shown in Figure 2.3(a), while Figure 2.3(b) shows return level curves for the expected magnitude of HDWI5x in the 2026 climate (red line) and a 1.3°C cooler climate without human-caused warming. In panel (a) the fitted model (black line) reflects the general trend in the data (green dashed line) well, while in panel (b) the points representing observed values generally lie close to the line, indicating that the model captures the distribution of the data reasonably well.

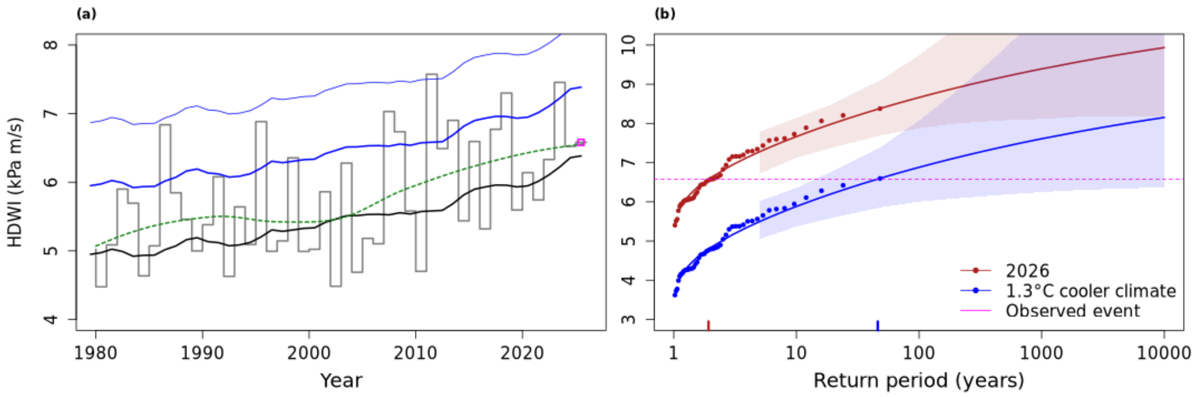

*Figure 2.3: **(a)** Annual time series of HDWI5x in the Patagonian study region, with fitted model overlaid. Solid black line denotes the expected 5-day peak HDWI each year, given the observed values of the smoothed GMST. Blue lines indicate the expected magnitude each year of a 1-in-6-year (thick line) and 1-in-40-year low rainfall event (thin line). Green dashed line is a nonparametric Loess smoother. 2025-26 value is highlighted with a magenta box. **(b)** Return level plots showing the expected magnitude of events of a given return period in the climate of 2026 (red) and a climate with 1.3ºC cooler climate (blue). Historic observations are shown twice: shifted to the current climate (red points) and shifted to the climate of the pre-industrial era (blue points). Shading regions indicate a bootstrapped 95% confidence interval. The magenta line shows the magnitude of the 2026 peak. All data: ERA5-Land.*

2.2.2 Trends in November-January precipitation

To identify which modes of variability contribute most to changes in NDJ precipitation in this region, we first fit a statistical model in which the log of the accumulated NDJ rainfall depends linearly on GMST and different combinations of ENSO and the detrended SAM. Estimated changes in the intensity of NDJ rainfall are shown in Table 2.7 along with the estimated return period of NDJ precipitation as low as that observed in 2025-2026 and the AIC, a measure of how well the model fits the data. In all four versions of the model, increased warming is consistently associated with a strong drying trend of 32-35%, indicating that this trend is robust to the choice of additional covariates. The current weak La Niña state is associated with a weak further reduction of 2-7%, while we would expect around 20% more precipitation due to the December 2025 SAM state.

In all variants, the 2025-26 low rainfall in this region was again only slightly unusual, with a return period of between 3-8 years, although it is more unusual when the recent SAM state is taken into account. Estimates of the probability ratio (the factor change in the likelihood of a November-January period as dry as 2025-2026) associated with 1.3 degrees of warming vary from 6-25 times as likely, depending on the model, but the uncertainty about all of these estimates is very high (Table A2.3). The AIC indicates that models that include the SAM fit the data much better than models with GMST alone, with the best fit obtained by including both GMST and SAM. Results for this model are discussed in detail below.

Covariates	**% change in NDJ precipitation**			**Return period**	**AIC**
	GMST	**ENSO**	**SAM**		
GMST only	-35 (-58.5, -3.46)	-	-	3.26 (1.65, 15.2)	147
GMST + ENSO	-31.9 (-57.8, 10.4)	-6.79 (-19.9, 6.29)	-	3.09 (1.55, 18.5)	147
GMST + SAM	-35 (-56.5, -2.99)	-	20.1 (5.46, 39.1)	8.12 (3.01, 124)	141
GMST + ENSO + SAM	-34 (-57.1, 5.14)	-2.21 (-16.2, 10.7)	19.3 (3.91, 38.7)	7.61 (2.77, 132)	143

Table 2.7: Change in intensity of NDJ precipitation in Patagonia region associated with each factor, estimated using different combinations of relevant covariates. AIC is a measure of how well each model fits the data, penalised by the number of parameters in the model to avoid over-fitting, with lower scores indicating a better fit. The model used in the attribution analysis is highlighted in yellow, while the model that fits the data best is shaded purple.

Because of the difficulty of obtaining time series of the SAM for climate models within the time frame of a rapid study, the full attribution analysis is carried out using a statistical model in which NDJ precipitation depends on GMST only, for an event with a return period of 5 years. Although this is not expected to capture all of the variability in the time series, we expect estimates of the mean GMST-dependent trend to be robust.

The fitted trend over time, given the values of the two covariates in each year, is shown in Figure 2.4(a). The fitted model (black line) captures the general trend in the data (green dashed line), although there is again some additional decadal variability not accounted for by the model, with 2000-2015 somewhat wetter than predicted. Corresponding plots showing the fitted model as a function of each covariate are shown in Figure A2.2. Figure 2.4(b) shows return level curves for the expected magnitude of NDJ precipitation in the 2026 climate (red line) and a 1.3°C cooler climate without human-caused warming. The points representing observed values generally lie close to the line, although the very lowest values are slightly underestimated. However, all points lie well within the 95% confidence intervals, indicating that the model captures the distribution of the data reasonably well.

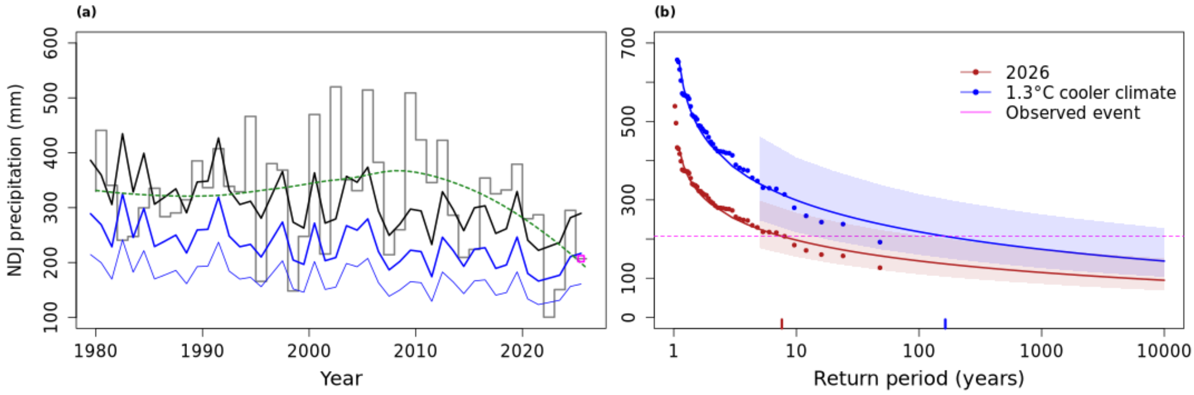

*Figure 2.4: **(a)** Annual time series of NDJ precipitation in the Patagonia study region, with fitted model overlaid. Solid black line denotes the expected NDJ precipitation each year, given the observed values of the smoothed GMST and December SAM index. Blue lines indicate the expected magnitude each year of a 1-in-6-year (thick line) and 1-in-40-year low rainfall event (thin line). Green dashed line is a nonparametric Loess smoother. 2025-26 value is highlighted with a magenta box. **(b)** Return level plots showing the expected magnitude of events of a given return period in the climate of 2026 (red) and a climate with 1.3ºC cooler climate (blue). Historic observations are shown twice: shifted to the current climate (red points) and shifted to the climate of the pre-industrial era (blue points). Shading regions indicate a bootstrapped 95% confidence interval. The magenta line shows the magnitude of the 2025-2026 NDJ rainfall. All data: ERA5-Land.*

2.2.3 Trends in effective precipitation

Alongside trends in NDJ precipitation, we again also briefly consider observed trends in effective precipitation, accounting for the drying effect of increasing temperatures.

Estimated changes in PET due to each factor are again consistent across all model variants, with around 6-8% more PET associated with 1.3°C of warming regardless of the influence of ENSO or the SAM; around 2% more PET is associated with the current ENSO state, and around 2% less with the December SAM state (Table 2.4). Table 2.8 shows the resulting expected change in daily effective precipitation (in mm) associated with each factor in each of the models. Once again, the changes are fairly robust across all four model variants, with an estimated 1.2-1.5mm (250-500%) less effective precipitation associated with 1.3°C of warming; 0.2-0.3mm (10-20%) less associated with the current weak La Niña state; and 0.5-0.6mm (25-27%) more effective precipitation due to the December SAM state. Again, we see that the drying trend discussed above is compounded by the further drying effect of increasing temperatures, further reducing available water in the region.

Covariates	NDJ 2026 (mm/day)	Change in NDJ effective precipitation (mm)			Return period	AIC
		GMST	ENSO	SAM		
GMST only	-1.74	*-1.45 (-2.74, -0.2)*	-	-	4.57 (2.37, 16.1)	154
GMST + ENSO		*-1.23 (-2.68, 0.246)*	*-0.334 (-0.904, 0.112)*	-	4.25 (2.12, 18.2)	154
GMST + SAM		*-1.45 (-2.67, -0.147)*	-	*0.642 (0.213, 1.13)*	13.2 (4.75, 202)	148
GMST + ENSO + SAM		*-1.34 (-2.62, 0.121)*	*-0.174 (-0.777, 0.327)*	*0.589 (0.0739, 1.1)*	11.4 (3.97, 229)	150

Table 2.8: Change in intensity of NDJ effective precipitation in Patagonia associated with each factor, estimated using different combinations of relevant covariates. AIC is a measure of how well each model fits the data, penalised by the number of parameters in the model to avoid over-fitting, with lower scores indicating a better fit. The model used in the attribution analysis is highlighted in yellow, while the model discussed in the text is shaded purple.

2.3 Summary of observed trends

This section has analysed historic trends in fire-conducive conditions (characterised by the hot-dry-windy index, HDWI) and low early summer (November-January) rainfall from 1979-2026 in two regions affected by severe wildfires in January 2026.

In Chile, we find that the 2-day peak HDWI is not a particularly extreme event in today's climate, with an estimated return period of 3-4 years. However, what would previously have been unusually extreme HDWI conditions are becoming substantially more likely due to human-caused warming, with the current ENSO and SAM states also contributing to a lesser extent. We also observe a drying trend in November-January precipitation in the region, with an estimated 40-50% less precipitation now than would have been expected in a 1.3°C cooler climate. While the current weak La Niña state is expected to enhance this drying effect, the current state of the SAM would usually be expected to bring more rainfall. The drying trend is further compounded by increased potential evapotranspiration as temperatures rise.

We see a similar pattern in Patagonia, where the observed 5-day peak HDWI is today not considered particularly extreme - particularly given the concurrent ENSO and SAM states, both of which would be expected to lead to lower HDWI - but would have been much rarer without the effect of human-caused climate change. The drying trend in this region is somewhat weaker than was observed in the Chile study region, but still striking, with an estimated 32-35% less precipitation expected today than in a 1.3°C cooler climate, and further drying from increased PET.

Due to operational constraints, this analysis uses only a single reanalysis dataset; furthermore, due to concerns about the quality of the data prior to the satellite era, the analysis only uses data from 1979 onwards. With such a short time series, some uncertainties - particularly around the contribution from modes of natural variability - are not well constrained. In the next section, we combine results from the observational dataset with results from a similar analysis for climate models.

3 Attribution of trends

3.1 Evaluation of climate models

The climate models are evaluated against the reanalysis in their ability to capture:

1. Seasonal cycles: For this, we qualitatively compare the seasonal cycles of temperature and precipitation based on model outputs against observations-based cycles. We discard any models that exhibit ill-defined peaks in their seasonal cycles.

2. Spatial patterns: Models that do not match the observations in terms of the large-scale summer (DJF) precipitation and temperature patterns are excluded.

3. Parameters of the fitted statistical models. We discard the model if the model and observation parameters ranges do not overlap.

Each model is labelled as ‘good’,’reasonable’, or ’bad’ in terms of the three criteria discussed above. A model is given an overall rating of ‘good’ if it is rated ‘good’ for all three characteristics. If there is at least one ‘reasonable’, then its overall rating will be ‘reasonable’ and ‘bad’ if there is at least one ‘bad’. We aim to use only ‘good’ models where possible, but for each framing or model setup we also include ‘reasonable’ models if we would otherwise retain fewer than five models.

In general, all of the models evaluated for this study showed an acceptable representation of the seasonal and spatial characteristics. Therefore, for rainfall, we adopted a stricter criteria and did not include models that were downscaled with RCA4, as these models showed a wider spatial extent in the rainfall than in the observations. Of 16 candidate models for HDWI, 9 were retained for Chile, and 12 for Patagonia. Of 18 candidate models for NDJ precipitation, 8 were retained for Chile and 5 for Patagonia. Tables of the model evaluation results can be found in Appendix A3.

3.2 Synthesis of results

For the HDWI and NDJ rainfall in the two regions defined above, we evaluate the influence of anthropogenic climate change on the events by calculating the probability ratio as well as the change in intensity using observations and climate models. We have also analysed the influence on La Niña, as well as the Southern Annular Mode (SAM), in reanalysis, as described in section 2.1.1. While including both improves the fit of the statistical model for the NDJ precipitation, the results on the influence of human-induced climate change is not sensitive to whether the co-variates are included, thus for the synthesis we use a statistical model based on GMST only. Models which do not pass the evaluation described above are excluded from the analysis. The aim is to synthesise results from models that pass the evaluation, along with the observations-based products, to give an overarching attribution statement. Tables of the results of this model fitting can be found in Appendix A4.

Figures 3.1 to 3.4 show the changes in probability and intensity for the observations (blue) and models (red). As only one reanalysis dataset is used the light and dark blue bars are identical. Before combining them into a synthesised assessment, a term to account for intermodel spread is added (in quadrature) to the natural variability of the models. This is shown in the figures as white boxes around the light red bars. The dark red bar shows the model average, consisting of a weighted mean using the (uncorrelated) uncertainties due to natural variability plus the term representing intermodel spread (i.e., the inverse square of the white bars).

Observation-based products and models are combined into a single result in two ways. Firstly, we neglect common model uncertainties beyond the intermodel spread that is depicted by the model average, and compute the weighted average of models (dark red bar) and observations (dark blue bar): this is indicated by the magenta bar. As, due to common model uncertainties, model uncertainty can be larger than the intermodel spread, secondly, we also show the more conservative estimate of an unweighted, direct average of observations (dark blue bar) and models (dark red bar) contributing 50% each, indicated by the white box around the magenta bar in the synthesis figures.

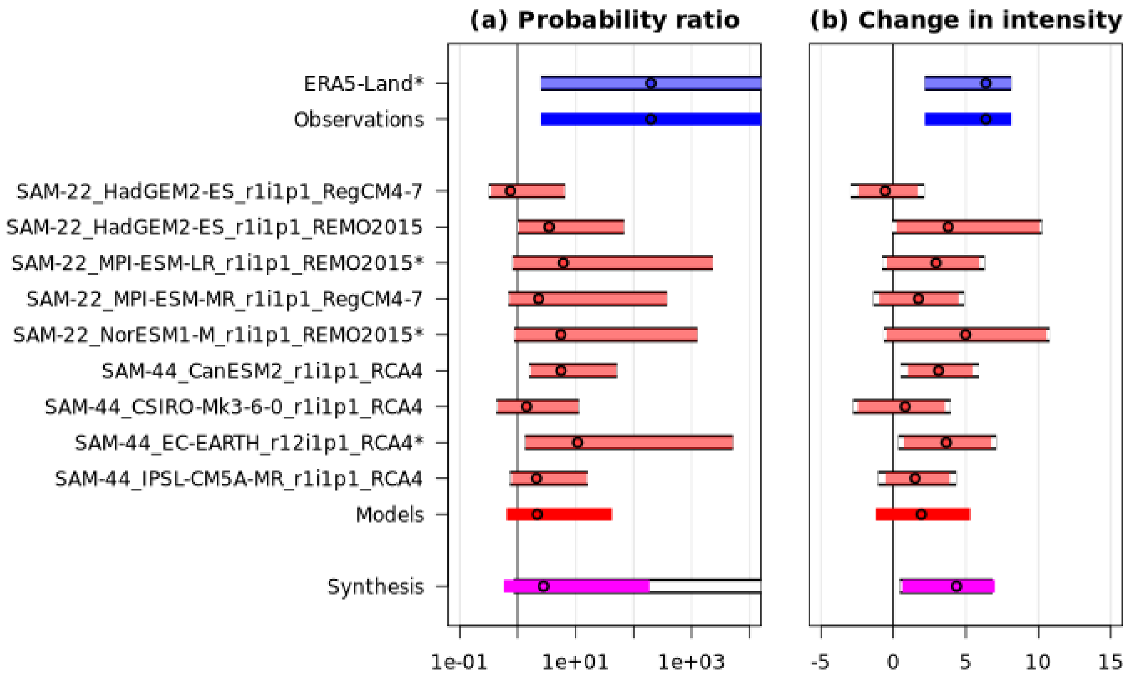

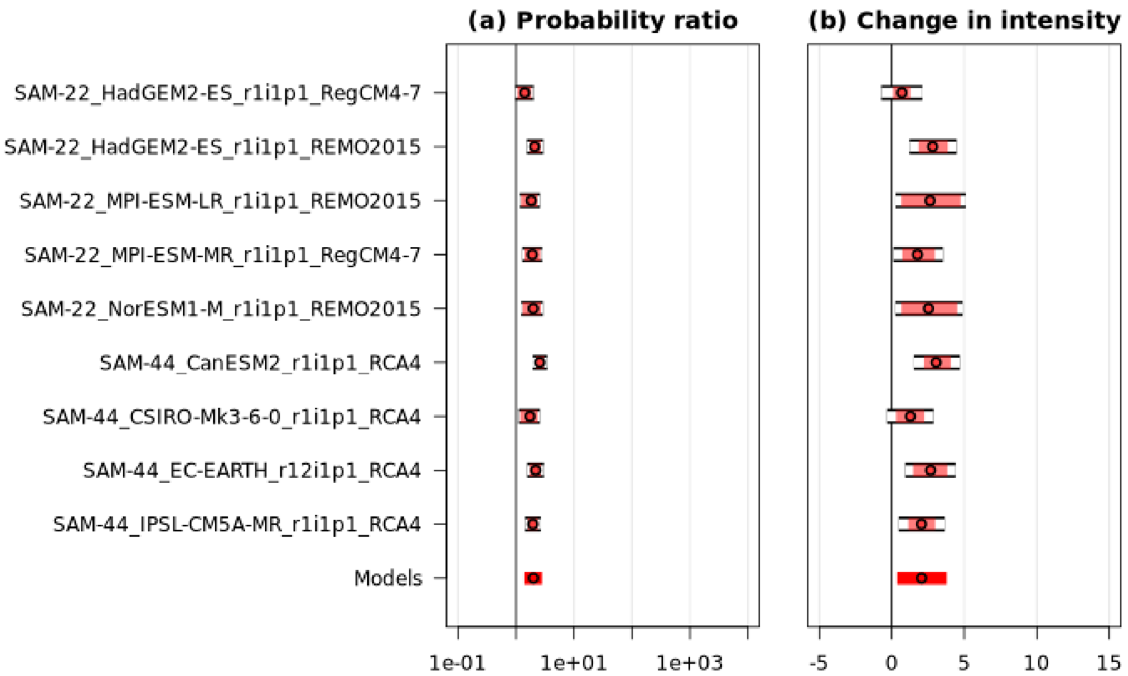

*Figure 3.1: Synthesis of changes in HDWI for Chile region when comparing (top row) the 2026 climate and a 1.3°C cooler climate representing the preindustrial past and (bottom row) the 2026 climate and a 1.3°C warmer climate. Change in intensity is given in kPa m/s. Probability ratios are truncated in the figures at 10000 for legibility. For models marked with * the upper bound of the probability ratio was infinite.*

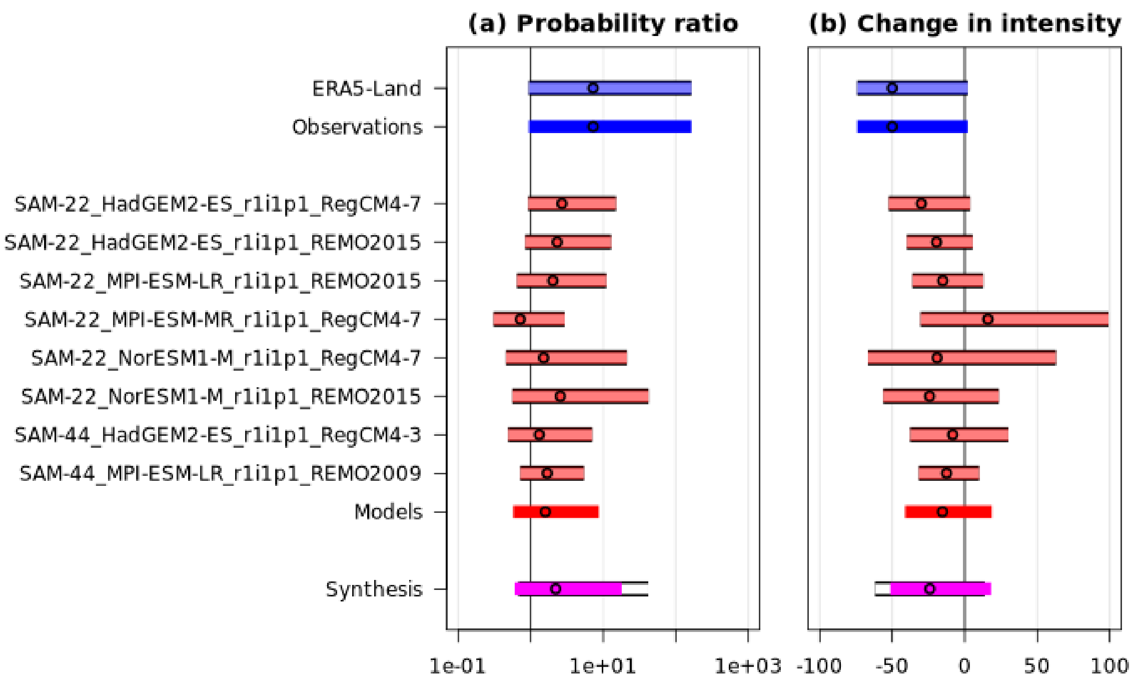

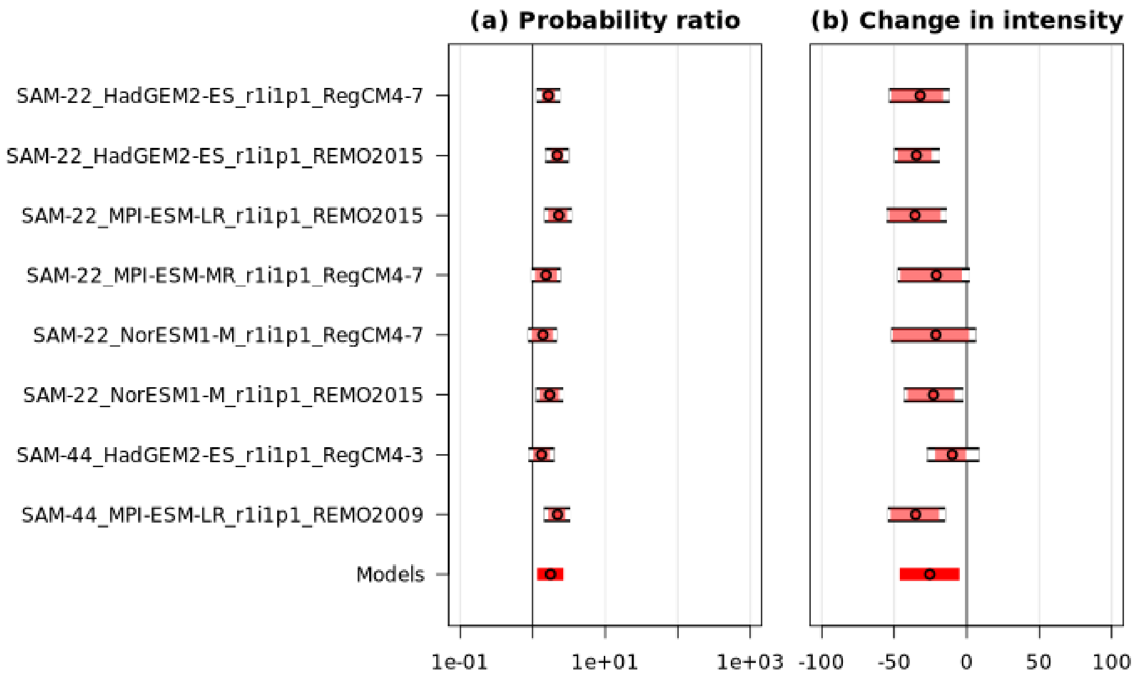

Figure 3.2: Synthesis of changes in NDJ precipitation for Chile region when comparing (top row) the 2026 climate and a 1.3°C cooler climate representing the preindustrial past and (bottom row) the 2026 climate and a 1.3°C warmer climate. The change in intensity is a relative change, given as a percentage.

Data		HDWI		NDJ rainfall	
		Probability ratio	**Intensity change (kPa m/s)**	**Probability ratio**	**Intensity change (%)**
Observations	**Past-Present**	**198 (2.53, ∞)**	**6.39 (2.17, 8.13)**	7.25 (0.945, 165)	-50 (-74.2, 2.14)
Models		2.18 (0.642, 42.5)	1.92 (-1.22, 5.3)	1.59 (0.576, 8.69)	-15.4 (-41.1, 18.7)
Synthesis		2.79 (0.583, 187)	**4.36 (0.589, 6.97)**	2.21 (0.598, 17.9)	-24 (-51.1, 18.2)
Models only	**Present-Future**	**2 (1.39, 2.83)**	**2.05 (0.368, 3.78)**	**1.76 (1.15, 2.66)**	**-25.4 (-46.2, -4.95)**

*Table 3.1: Summary of results for attributable changes in HDWI and NDJ precipitation in Chile, presented in Figures 3.1-3.2: associated with 1.3°C of warming from the preindustrial climate to 2026 (past-present) and with a further 1.3°C of warming (present-future, using climate models only). Numbers in brackets indicate 95% confidence intervals. Statistically significant changes, indicating a particularly strong signal that has emerged from the natural variability in the time series, are highlighted in **bold** font.*

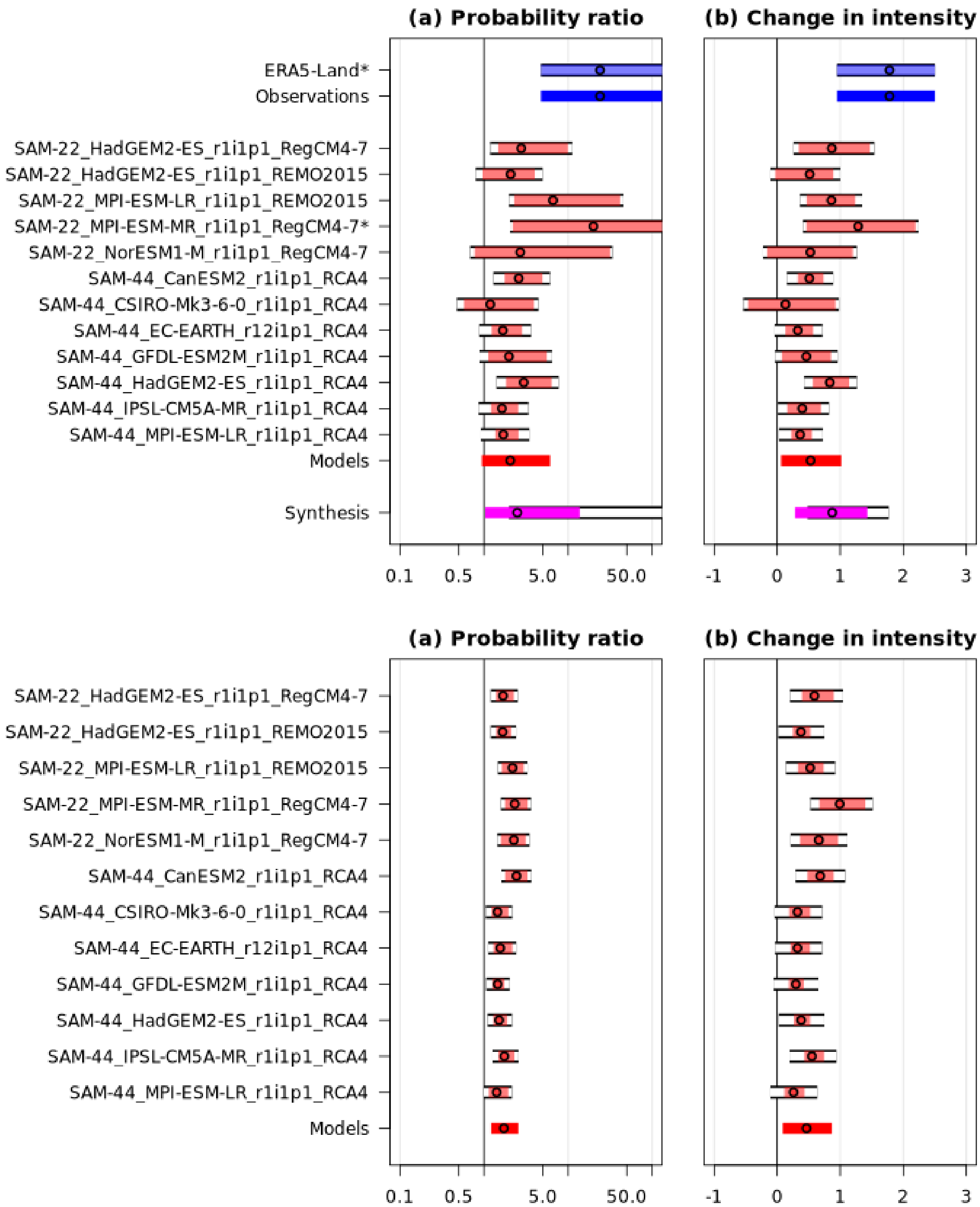

*Figure 3.3: Synthesis of changes in HDWI for Patagonia region when comparing (top row) the 2026 climate and a 1.3°C cooler climate representing the preindustrial past and (bottom row) the 2026 climate and a 1.3°C warmer climate. Change in intensity is given in kPa m/s. Probability ratios are truncated in the figures at 100 for legibility. For models marked with * the upper bound of the probability ratio was infinite.*

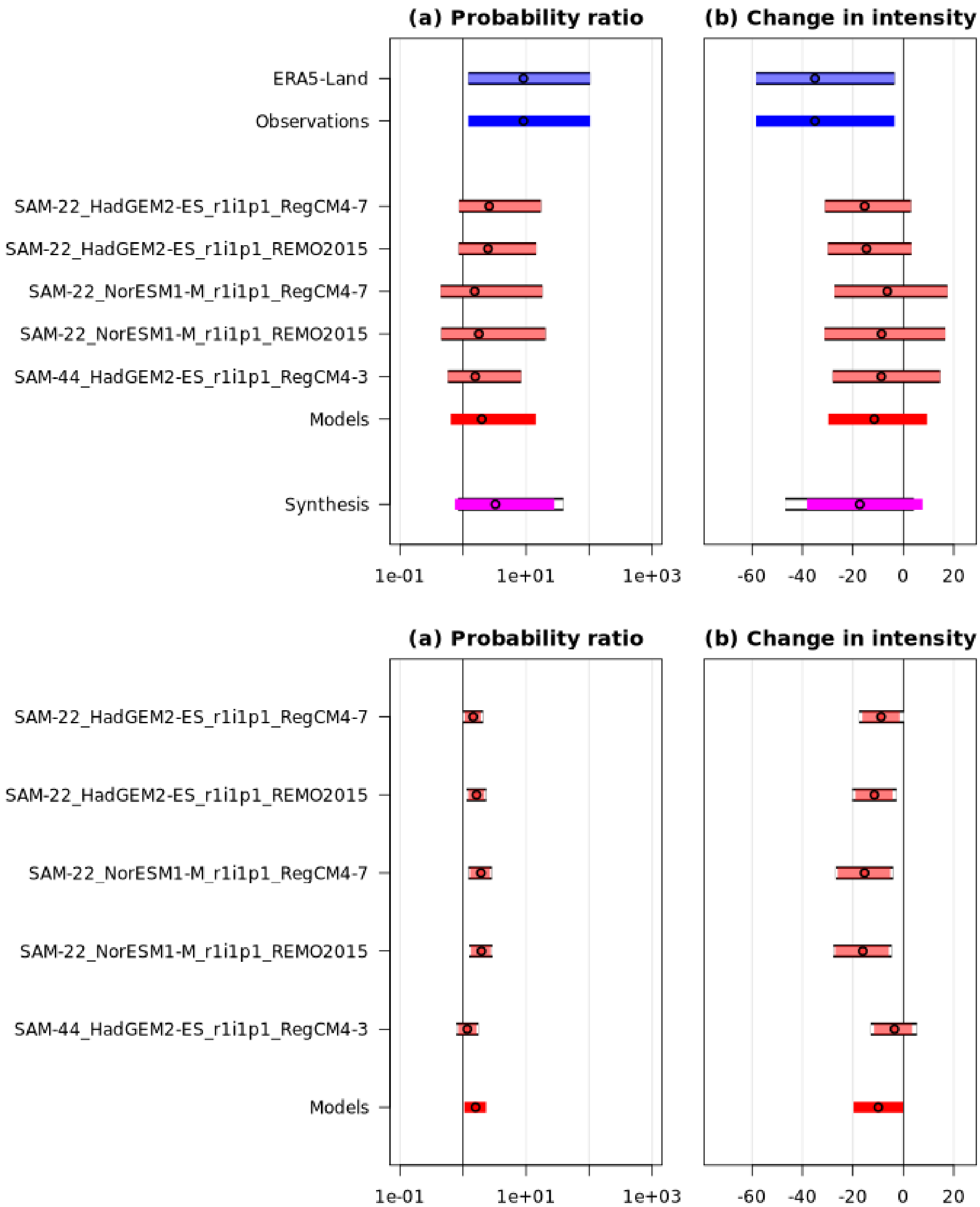

Figure 3.4: Synthesis of changes in NDJ precipitation for Patagonia region when comparing (top row) the 2026 climate and a 1.3°C cooler climate representing the preindustrial past and (bottom row) the 2026 climate and a 1.3°C warmer climate. The change in intensity is a relative change, given as a percentage.

Data		HDWI		NDJ precipitation	
		Probability ratio (95% CI)	**Intensity change (95% CI)**	**Probability ratio (95% CI)**	**Intensity change (95% CI)**
Observations	**Past-Present**	**24 (4.77, 3050)**	**1.78 (0.947, 2.5)**	**9.08 (1.22, 104)**	**-35 (-58.5, -3.46)**
Models		2.05 (0.941, 6.13)	**0.529 (0.063, 1.02)**	1.98 (0.639, 14.4)	-11.5 (-29.8, 9.47)
Synthesis		**2.49 (1.04, 13.7)**	**0.871 (0.281, 1.43)**	3.27 (0.746, 27.8)	-17.3 (-38.2, 7.7)
Models only	**Present-Future**	**1.73 (1.21, 2.57)**	**0.465 (0.086, 0.865)**	**1.58 (1.06, 2.32)**	**-9.91 (-19.7, -0.192)**

*Table 3.2: Summary of results for attributable changes in HDWI and NDJ precipitation in Patagonia, presented in Figures 3.3-3.4: associated with 1.3°C of warming from the preindustrial climate to 2026 (past-present) and with a further 1.3°C of warming (present-future, using climate models only). Numbers in brackets indicate 95% confidence intervals. Statistically significant changes, indicating a particularly strong signal that has emerged from the natural variability in the time series, are highlighted in **bold** font.*

In both regions the changes in observations are stronger than in the models. However, owing to the data required to calculate the HDWI, we are only using one "observational" product - the ERA5-Land reanalysis - and so we cannot assess the quality of the observations by comparing to other observation based data products and thus do not give them higher weight than the climate models (thus do not communicate the white bar around the magenta synthesis).

The climate models used performed on average relatively well (see section 3.1) and show the same trend as the reanalysis data. There is remarkably good agreement between the models in all cases. This is also true for the assessment of the same indices and variables in a 1.3C warmer climate from today when all changes are statistically significant and in the same direction as in the attribution results, showing a further decrease in the intensity of rainfall by 25% in the Chilean region and about 10% in the Patagonia region. This consistency between models and into the future gives high confidence that the observed changes are indeed driven by climate change.

For the Chilean region, the synthesised results are an increase in the likelihood of the 2-day HDWI of a factor of 2.8 (0.56, 187) and an increase in intensity of 4.36 (0.6, 7). The seasonal precipitation (NDJ) in the same region is decreasing by a factor of 2.2 (0.6, 18) and decreasing in intensity by 24% (-51%, 18%) (Table 3.1).

For the Patagonia region, the synthesised results are an increase in the likelihood of the 5-day HDWI of a factor of 2.5 (1, 13.7) and an increase in intensity of 0.9 (0.3, 1.4). The seasonal precipitation (NDJ) in the same region is decreasing by a factor of 3.3 (0.7, 27.8) and decreasing in intensity by 17.3% (-38.2%, 7.7%) (Table 3.2).

3.3 Conclusions

Combining lines of evidence from the observations and synthesis of changes in the past climate, results from future projections, and physical knowledge, we communicate the rounded best estimate of the synthesis as an increase in the likelihood of fire weather conditions as extreme as those observed in January 2026 by a factor of about 3 in Chile (2-day HDWI) and by a factor of about 2.5 in Patagonia (5-day HDWI). The decrease in the intensity of seasonal rainfall due to human-caused warming is about 25% in the Chilean region, and in the Patagonia region about 20%.

4 Vulnerability and exposure

Wildfires erupted across the Andean foothills of central-southern Chile, and Argentina and Chile's Patagonian regions, in early to mid-January 2026, affecting a landscape characterized by dense native forests, national parks, and small rural and tourist communities along the Chile-Argentina border. In Argentina, fires began in early January in Patagonia's Chubut province, and reignited by 27 January, spreading near Cholila, Puerto Patriada, El Hoyo, El Bolson, and Lago Puelo. These affected areas lie along the eastern slopes of the Andes, close to the Chilean border, and are marked by forested valleys, glacial lakes, and popular tourism hubs, increasing both exposure and evacuation pressures (IFRC, 2026).

In Chile, outbreaks ignited on 14 December and escalated to large-scale fires on 16 January in the Biobio and Ñuble regions, and spread rapidly south and east through La Araucania, Maule, and the Metropolitana regions, affecting areas such as Monte Negro, Codihue, and Angol (ECHO, 2026a). These regions encompass a mix of coastal ranges, valleys, and forested slopes where settlements are located on wildland-urban interfaces.

The fires were fuelled by temperatures exceeding 38C, prolonged drought conditions, and strong winds of 40-50 km/h, which drove rapid fire spread and, in some locations, the formation of pyrocumulus clouds. In Chile, where the President has declared a state of catastrophe[1] (Ministerio del Interior, 2026), the wildfires destroyed at least 1,000 homes, killed 23, injured hundreds, and prompted over 52,000 evacuations (Chile UN, 2026; ERCC, 2026; GDACS, 2026). As of 23 January, over 64,000 hectares had burnt nationwide (OCHA, 2026). In Argentine Patagonia, where the national government has likewise declared a state of emergency[2], over 45,000 hectares has burnt by 21 January, triggering the evacuation of at least 3,000 people, primarily tourists and residents from areas including El Hoyo, Puerto Patrida, and Epuyén (Sanchez, 2026; ECHO, 2026b).

Beyond serving as points of comparison, these events also demonstrate that the extent of area burned does not necessarily correlate with societal impacts such as mortality, displacement, or shelter loss. Chile's 2017 wildfires burned over 452,000 hectares nationwide resulting in 11 deaths and over 1,500 homes lost (Pliscoff et al., 2020). In Argentina's Patagonian provinces, the 2021 fires burned about 15,000 hectares across similar transboundary landscapes, but with fewer evacuations, estimated to approximately 5,000. Chile experienced more devastating fires in 2023-2024 in the urbanized Valparaiso region, where at least 138 people died despite a comparatively smaller burned area of about 26,000 hectares (ACAPS, 2024). Rather, these outcomes are largely determined by the spatial coincidence of fire with population density, settlement type, and land-use patterns, underlying social vulnerability, and the effectiveness of risk governance and emergency response systems. Accordingly, this chapter focuses on factors of vulnerability, exposure, and coping capacity that both drove and mitigated fire risk and impacts in relation to the 2026 fires.

[1] A constitutionally defined emergency for major disasters which centralizes authority and permits strict limits on movement, assembly, and property to restore order and manage the crisis.

[2] A statutory emergency framework focused on coordination, funding, and response support, typically involving lighter restrictions on rights and civilian-led control

4.1 Eco-system, landscape and fuel availability

In the Chilean regions of Biobío, Ñuble, Maule, Araucanía, and Los Ríos, as well as the southern provinces of Osorno and Palena, along with the neighboring Argentinean provinces of Chubut and Río Negro, the ecological landscape is characterized by temperate forest systems comprising a mix of broadleaf and conifer species, montane forests, and wetlands at higher elevations (FIRE-RES 2021). This region comprises coexisting Mediterranean shrublands and sclerophyllous forests alongside temperate deciduous forests, making it globally significant for its rich biodiversity and high levels of endemism (Gomez-Gonzales et al., 2025). These landscapes sustain diverse ecosystems and many endemic or range-restricted species. However, they are threatened by land-use change, fragmentation, and climate disturbances. In recent decades, large-scale industrial plantations of Eucalyptus and Pinus—characterized by uniform structure and composition—have expanded rapidly, replacing more diverse landscapes and transforming the area into an anthropogenic environment (Heylmayr et al. 2016; Gajardo et al. 2025). These exotic species increase fire risk by altering fuel, endangering native forests (Franzese et al., 2022; Leal-Medina et al., 2024)

The region's ecological vulnerability to wildfire is high due to dense fuel loads, varied vegetation structure, and complex terrain that can focus fires in valleys and ridges; rising temperatures, longer dry periods, and shifting precipitation patterns caused by climate variability and change are increasing the frequency and length of fire seasons, raising the threat to biodiversity and ecosystem services such as water regulation, soil stability, and carbon storage (Kitzberger et al., 2022).

Fires in Patagonia not only devastate thousands of hectares of native forests and grasslands but also place immense pressure on biodiversity. Endemic species listed as vulnerable by the International Union for Conservation of Nature (IUCN) face threats from habitat destruction and an increasing risk of extinction (Lazo-Cancino et al., 2020). The fires are also threatening Los Alerces National Park, a UNESCO World Heritage Site known for its ancient alerce trees which can live for more than 3,600 years (UNESCO, n.d.). These fires underscore the effects of budget cuts to environmental management, as the park covers more than 259,000 hectares and is home to endemic species, including the endangered huemul, the pudú and the Alerces frog (Sistema de Información de Biodiversidad, 2026). Soil damage is particularly severe in these Patagonian regions, and recovery after large-scale fires can take decades or even centuries (Mallikarjun et al., 2025). Fires destroy the surface organic layer, leading to degradation and erosion that hamper natural plant regeneration. Without this humus layer to retain moisture and nutrients, ecological succession slows, seedling growth is limited, and the land becomes more susceptible to desertification (Vieira et al., 2026; Zhou et al., 2025).

4.2 Sociodemographics

A study (Veloso, 2025) conducted in South-Central parts of Chile on improving wildfire resilience in the region highlights the critical role of social and institutional factors in shaping wildfire risks and people's vulnerabilities to its impact. The research found that 74.5% of survey respondents identified lack of appropriate education and awareness about wildfires as a primary contributor to wildfire occurrences in the region. This also suggests that insufficient awareness and public knowledge regarding early warning signs, response measures and preventive techniques have the potential to exacerbate the severity and frequency of these events. Further, an overwhelming 96.4% of respondents mentioned that wildfires had a substantial impact on their place of residence, underscoring the widespread vulnerability of communities in the region, especially in the WUI region (Ibid).

4.2.1 Health

Wildfires have a significant impact on health, smoke contains a mixture of hazardous air pollutants, such as fine particulate matter, Nitrogen dioxide, ozone, aromatic hydrocarbons that are propagated through large distances beyond the zone of the wildfires (WHO, n.d.; Camargo et al., 2024). The main impacts are associated with increased cases of respiratory illnesses including asthma attacks, cardiovascular complications, increased risk of heart attacks, strokes and irregular heart rhythms, especially in people with pre-existing heart conditions. It also has adverse effects on long-term respiratory diseases including lung cancer and mental health (Camargo et al., 2024). Wildfires affect animals' habitat and force them to relocate and move to places away from fires and near humans, exacerbating the risk of zoonotic diseases like hantavirus (Garces et al., 2023).

A study from Arrizaga et al. (2023) analyzed data of 15 wildfire seasons (2004-2018) in Chile, matched with granular (intra-day) records of wind direction and air quality and administrative records of hospitalizations, found that exposure to large fires increase an average of 10% PM2.5 concentration in municipalities up to 200km from the wildfire. The exposure to upwind wildfires increased rates of hospitalizations for respiratory causes, especially in children as they are scientifically prone to inhaling more air than their body weight (Slavik, 2023; Arrizaga et al., 2023). Another study on the impact of wildfire smoke on children's respiratory health in Santiago and Valparaiso, Chile (2010 to 2013) found an increase in respiratory diseases (bronchitis, chronic lower respiratory diseases and pneumonia) (Ciciretti et al., 2021). Prolonged exposure to smoke leads to adverse pregnancy outcomes such as pre-term birth, low birth weight and complications arising from respiratory problems (Slavik, 2023). Moreover, delayed effects of exposure to wildfires increased respiratory hospitalization among elderly, exacerbating pre-existing respiratory conditions (Arrizaga et al., 2023). Older adults also face significant mobility restrictions, disruptions in normal health routine including medication and check-ups, limited access to disaster preparedness, thereby further increasing their vulnerabilities (Melton et al., 2023).

During the 2026 emergency, the Ministry of Health of Chile has reported 857 health emergencies and 7 patients affected with severe burns, since January 18th. They have shared recommendations around safe water consumption, reducing exposure to smoke and how to prevent hantavirus. It is important to highlight that in 2025 Chile reported 44 cases of hantavirus and 8 deaths because of it (Ministry of Health Chile, 2026).

In the case of Argentina, a study after wildfires in the Paraná River Delta departments surrounding Rosario, Argentina (2021–2022) showed that increased PM2.5 concentrations in this city is associated with higher risk of ST-elevation myocardial infarction and hospitalizations (Huespe et al., 2024). During the 2026 emergency, the Argentinian Respiratory Medical Association and the Argentinian Pediatric Society warned about the respiratory problems in the population with special concern about children and pregnant women, highlighting the risk of a sanitary emergency (La Nacion, 2026). The government of Chubut province has shared recommendations to prevent health impacts and have provided medical attention to the affected population and responders of the fires (Gobierno del Chubut, 2026).

4.2.2 Livelihoods

Livelihoods of indigenous communities are intrinsically interwoven with forest related activities; as a consequence, wildfire events place severe strain on the socioeconomic resilience of these populations. Beyond physical destruction, high-intensity wildfires undermine agricultural livelihoods, halt market operations during evacuations and power outages, and leave enduring psychological impacts on communities (Dillis et al., 2022; O'Hara et al., 2021; Zakowski et al.,2023; Pinzón et al., 2025). In Argentina, the large-scale expansion of exotic forest plantations—primarily pine—has produced homogeneous landscapes characterized by high flammability. At the same time, agricultural frontier expansion and the degradation of native forests have disrupted historical fire regimes, shifting from sporadic fire events toward large-scale, high-severity megafires (Cavallero et al., 2023).

Agriculture is a critical livelihood sector in Chile and Argentina, but it is also increasingly exposed to and affected by wildfire risk. In Chile, small-scale farmers account for approximately 90% of agricultural production, making rural livelihoods highly sensitive to climate-related shocks (FAO, 2021). An FAO (2021) case study highlights that wildfires have significantly affected agricultural activities, with rising frequency and intensity disrupting farming systems through the destruction of crops, pasturelands, livestock, and forestry resources, leading to income losses and prolonged recovery periods.

This rising wildfire risk is partly driven by the expansion of rainfed crops and plantation forestry into drought-prone areas and the increasing overlap of agricultural, forestry, and residential land uses in the wildland-urban interface (WUI), which increase fuel availability and ignition potential (FAO, 2021). Meanwhile, diversified farming systems such as agroforestry, along with effective grazing, residue management, firebreak maintenance, and the integration of wildfire into agricultural risk planning, can reduce fuel loads while limiting fire spread, thereby lowering impacts on farms and rural livelihoods.

Extensive grazing systems, such as those used by Puestero communities, are particularly exposed to wildfire impacts due to rangeland degradation, forage loss, and reduced livestock productivity (Fry et al., 2013). Evidence from other fire-prone regions, including southern Amazonia, further shows that forest-to-agriculture conversion combined with repeated fires can cause long-lasting soil degradation, with declines in key soil health indicators persisting for nearly a decade after fire events (Naval et al.,2025).

More prominently in the summer of 2017, the wildfires affected more than 500,000 hectares of agricultural land. Agriculture serves as a primary livelihood in Chile's rural areas, home to 25.5% of the country's population (FAO, 2021). Such a disproportionate impact of wildfire on indigenous communities is also evident during the 2023-2024 wildfire episodes in the Brazilian State of Amazonas, around 4,000 people across 24 indigenous communities were impacted with dwindling food security, livelihood loss and mobility restrictions (Jones et al., 2024). Other devastating wildfire events have burned millions of hectares of land across California (2017), Greece (2018), the Amazon

(2019), and Australia (2019–2020) with profound and far-reaching impacts on ecosystems, livelihoods, and economies, highlighting wildfires as an increasingly significant global risk intensified by climate change and land-use pressures (FAO, 2021). However, in the Chilean context, it is interesting to note that agriculture is inadequately represented within the country's National DRM policy, with limited sector-specific measures included (FAO, 2021). Moreover, despite employing a substantial share of the national workforce, the agricultural sector is not represented in the National Emergency Committees. However, the Ministry of Agriculture (MINAGRI) is a member of several working groups of the National DRR Platform (FAO, 2021).

In response to the wildfire event, MINAGRI together with the Agriculture Development Institute in Chile and regional delegates announced an agricultural emergency in the Ñuble region and provided direct support to around ten families that suffered severe losses (Freshplaza, 2026). While the government agencies and regional authorities have supplied immediate aids like animal feed and beekeeping supplies, to stabilize affected livelihoods, longer-term recovery and resilience measures are likely to be needed. On the Argentina side of the Patagonia region, wildfires have already devastated more than 230,000 hectares of forest, forcing the evacuation of households and tourists (Sanchez, 2026; ECHO, 2026b). These extensive forested areas also constitute a primary source of livelihood for several indigenous communities.

These impacts are further aided by budget cuts and deregulation in Argentina's national park system. As tourist numbers increase, forest rangers report that reduced resources have made it increasingly difficult to monitor fire hazards, clear trails, and educate visitors on park stewardship. In March, the government also removed mandatory licensing requirements for guides overseeing high-risk tourism activities such as glacier trekking and rock climbing in Los Alerces National Park, weakening rangers' capacity to effectively manage evacuations and respond to fire-related risks (La Nacion, 2026).

4.3 Wildland-built environment interface

Wildland-urban/built environment (WUI) interface in Andean Patagonia has become one of the most dynamic and fire-exposed zones in South America, where rapid and unplanned housing expansion in wilderness areas dispersed infrastructure, and changing climate jointly amplify wildfire risk (Godoy et al., 2022). Recent wildfires in Chile and Argentina have threatened or directly affected several urban and peri-urban neighborhoods, particularly in Patagonia and central-southern regions. In Chile alone, the WUI in the past few decades have increased to around 900km², thereby signalling the steady spread of human infrastructure into rural areas (Sariccolea, 2016; Veloso, 2025). This also indicates that alterations in traditional land-use systems and close proximity to agricultural land heighten risks of wildfire impacting communities settled around the areas.

The WUI areas increasingly host a mix of permanent residents, second-home owners, tourism infrastructure (cabins, campgrounds, small hotels), and Indigenous and rural communities living in scattered wooden houses embedded in native forest and shrublands in Argentina. As population has grown, more narrow, winding roads and new power lines have been installed through flammable forest, with lines often in contact with tree branches and reported as frequent ignition sources on windy days (Bachfischer et al., 2022).

In Chile, the blazes in the Ñuble and Biobio regions – about 500 kilometers (310 miles) south of the capital Santiago – have destroyed or damaged around 1,000 homes (Le Monde, 2026). In the cities of Penco and Lirquen, just north of Concepción, which have a combined population of 60,000, 1,000 homes destroyed or damaged and entire neighborhoods reduced to rubble, with melted cars and twisted metal widespread (BBC, 2026).

In Argentina fires affected mainly Chubut and Río Negro provinces, where peri-urban areas of the Cholila town besieged, with volunteer brigades defending homes and road closures on Route 40 which became a fire corridor (El Pais, 2026). In touristic destinations such as Epuyén and Puerto Patriada (in Chubut) flames advanced on neighborhoods like Pirque Hill, more than 3,000 people were evacuated, and dozens of homes destroyed in WUI zones (AP News, 2026).

The impact of the wildfires on the WUI underscore the need for risk-informed urbanization and infrastructure development to mitigate escalating fire threats. A recent study finds a 35.6% global WUI increase since 2000 (to 1.93 million km² by 2020), driven primarily by urbanization, which heightens fire exposure near communities; they urge fuel-aware urban planning and resource allocation within 3 km of WUI edges (Guo et al., 2024). To mitigate the risk in WUI, a tridimensional governance framework is recommended which includes integrating biophysical mapping (e.g., ember buffers[3]) with policy to guide resilient infrastructure and applying risk informed zoning practices (Cappelluti et al., 2025).

4.4 Wildfire risk management

4.4.1 Governance

Patagonia spans Argentina and Chile, with fire risk management overseen by a network of national and regional agencies that share responsibilities for prevention, suppression, and recovery. In Argentina, the main stakeholders include the National Fire Management Service (via the Federal Emergency Management Agency), provincial forestry directorates, civil defense authorities, emergency management ministries, local volunteer and fire brigades, local and provincial civil defense directorates and their brigades, and federal support by brigades from other provinces, including Buenos Aires and Santa Fe, among others. In Chile, civil protection and emergency response are overseen by the Ministry of the Interior and Public Security, with support from regional prefectures, the National Forest Service (CONAF), and regional firefighting and environmental health teams. Both nations rely on meteorological agencies—Argentina's Servicio Meteorológico Nacional and Chile's Dirección Meteorológica de Chile—for fire-weather predictions, drought monitoring, and alerts. Additionally, agriculture and ranching ministries provide guidance on land use and ignition hazards. Local governments, municipal fire brigades, forestry rangers, and community groups also engage with rural areas, Indigenous communities, and private landowners, forming a layered network from local to national levels.

Coordination takes place through formal incident command systems, cross-border liaison mechanisms, and shared information platforms. Joint task forces and incident management teams handle

[3] "Ember buffers" or "Zone 0," is a 1.50 meter critical noncombustible perimeter around a home designed to stop wildfire ignition from flying embers, which cause most structure losses thereby enabling the rapid.

suppression efforts, evacuation planning, and resource sharing. Cross-border communication is facilitated by bilateral emergency agreements, joint training, and mutual-aid arrangements, enabling quick deployment of personnel, equipment, and technology across provinces and regions. Information exchanges, common risk dashboards, and standardized incident reports support coordinated responses, while national platforms oversee seasonal burn bans, prescribed-burning guidelines, and public-awareness efforts. However, governance challenges persist. Fragmented mandates among national ministries and provincial or regional authorities can slow decision-making or obscure accountability. Data fragmentation, incompatible reporting standards, and limited interoperable infrastructure hinder real-time situational awareness, especially in cross-border zones of the Andes. Political priorities, land-use pressures, private concessions, and Indigenous rights complicate efforts to suppress and prevent. Although authorities generally recognize underlying causes—such as drought, ignition sources, and human activity—their knowledge of prevention best practices and enforcement varies. Strong awareness fosters proactive campaigns, regional risk planning, and disciplined enforcement; weaker awareness leads to reactive responses and uneven outreach. Overall, Argentina and Chile are working to enhance cross-border governance, data sharing, and preventive measures to lower Patagonia's fire risk.

4.4.2. Early warning systems - detection and communication

The wildfires that occurred in Argentina and Chile prompted the activation of both internal government alerts and public warning mechanisms, revealing notable advances and persistent limitations in early warning systems and disaster risk management frameworks. In both countries, information dissemination followed differentiated pathways for authorities and the general population, resulting in varying degrees of coverage, accessibility, and operational effectiveness.

In Argentina, the National Meteorological Service (Servicio Meteorológico Nacional, SMN) and the National Fire Management Service (Servicio Nacional de Manejo del Fuego, SNMF) issued official alerts indicating extreme wildfire danger during the summer season. These alerts identified critical conditions affecting 16 provinces during January and February, leading to strict restrictions on the use of fire and heightened surveillance in high-risk areas. While general alerts were publicly accessible and disseminated through official communication channels, detailed technical information—such as risk maps, operational analyses, and resource allocation planning—was primarily restricted to governmental institutions and specialized firefighting brigades (Infobae, 2026; Ministerio de Seguridad Nacional,2026).

The Argentine system is federalized, leading to heterogeneity among provinces in monitoring, detection, and response capacities, resulting in uneven preparedness levels. In many regions, wildfire detection relies heavily on satellite imagery, which often identifies active fires only after they have reached a significant spatial extent. Furthermore, the national mass alert system, AlertAR—approved in 2025 to enable georeferenced emergency notifications to mobile phones (ENACOM, 2025)—remains in its early stages of implementation. This limits the system's ability to deliver timely, direct warnings to populations exposed to rapidly evolving fire events (LaNacion, 2025).

Chile's wildfire alert system demonstrates a high degree of institutional integration and operational coordination (Preventionweb, 2025). The National Disaster Prevention and Response Service

(Servicio Nacional de Prevención y Respuesta ante Desastres, SENAPRED) and the National Forestry Corporation (Corporación Nacional Forestal, CONAF) activated early warning systems, red alerts, and preventive communications, targeting both authorities and the general public. A central component of Chile's preventive framework is CONAF's Botón Rojo (Red Button), a decision-support tool that identifies territories with a high probability of wildfire ignition or rapid spread (CONAF, 2024). Public-facing information included interactive risk maps and real-time situation reports, while emergency response teams accessed internal technical data to support operational decision-making.

Chile also operates the Emergency Alert System (Sistema de Alerta de Emergencias, SAE) for mobile phones (GSMA,2025), which has demonstrated high effectiveness. During wildfire events, SAE messages facilitated the evacuation of more than 50,000 individuals (Chile UN,2016).

Nevertheless, critical limitations persist within the Chilean context. In compound-hazard scenarios characterized by prolonged drought, extreme temperatures, and intense winds, fire spread dynamics may exceed the anticipatory capacity of existing alert systems in the future (Gil et al., 2024).

4.4.3 Policies, legislation and plans

Chile's National System for Disaster Prevention and Response (SENAPRED) was established in 2021 by law N° 21364, it is responsible for planning and implementing DRM in the country (Troncoso & Berwart, 2025). In this role, SENAPRED developed the National Policy for DRR 2020-2030 to provide a framework for public institutions, the scientific community, and civil society to integrate DRM objectives in alignment with international frameworks such as the Sendai Framework and the 2030 Agenda for Sustainable Development (Troncoso & Berwart, 2025). In the context of wildfires, the National Forestry Corporation set the Forest Fire Protection Program under its 2022-2026 strategic plan, establishing a model around prevention, mitigation, preparedness for response, and response. It also articulates with the Committee for Disaster Risk Management (COGRID in Spanish) at national, regional, communal and provincial level (Conaf, 2022). Last year, president Boric presented the National Action Plan for prevention, mitigation and control of wildfires for 2025-2026, it highlights an increase in the budget that will allow carry out different activities across the territory (Gob Chile, 2025). It also incorporates the Comprehensive Technological System for the Prevention and Control of Forest Fires where tools like "Botón Rojo" for forecast and monitoring and "Golpe único" for early rapid response to fires (Gob Chile, 2025). In addition to these policies, there are specific action plans and emergency plans that are designed at regional level. For instance, Biobío and Ñuble region presented their action plans in October 2025, outlining preparedness actions, investments in capacity building and operation of helicopters and planes to respond to the emergency (Conaf, 2025; Conaf, 2025).

The country has presented the Law for Wildfires and has been approved by the Senate this past January and is still waiting for a third constitutional stage in the Chamber of Deputies (Conaf, 2026). When approved, the law will focus on establishing a budget, primarily allocated to oversight and preventative measures, classifying the country into low, medium, high, or critical risk zones, work on preparedness for fires, establishing buffer zones to slow or halt the spread of fire (Gob Chile, 2026).

In Argentina, the National System for Comprehensive Risk Management (SINAGIR), created in October 2016 (by Law 27287) is in charge of integrate actions and coordinate the functioning of national government agencies, provincial governments, the government of the Autonomous City of

Buenos Aires and municipal governments, in order to strengthen and optimize actions aimed at risk reduction, crisis management and recovery (Ministerio de Seguridad Nacional, n.d.). It comprises the National Council for Comprehensive Risk Management and Civil Protection, the Federal Council for Comprehensive Risk Management and Civil Protection, the Executive Secretariat, and the Network of Scientific and Technical Organizations for Disaster Risk Management (Ministerio de Seguridad Nacional, n.d.). In 2025, the Federal Agency of Emergencies (AFE in Spanish) was created to respond to disasters and coordinate preparedness, response and recovery actions. In the context of wildfires, the Law of Fire Management (Law 26815) establishes national minimum environmental protection standards and budget for forest and rural fires within the national territory and regulates actions and operations for the prevention, pre-suppression and fighting of forest and rural fires (Ministerio de Justicia, 2012). In addition, the National Service for Fire Management (SNMF) is in charge of coordinating the resources required to combat forest, rural or interface fires, handling as well the Federal System for Fire Management (Ministerio de Seguridad Nacional, n.d.). On January 29th 2026, about 3 weeks after the start of the fires, president Milei declared emergency (Decreto 73/2026) in Chubut, Río Negro, Neuquén and La Pampa provinces, and in January 31st, Santa Cruz province was included as well (Decreto 80/2026). This includes urgent measures to stop wildfires and coordinate and implement a plan for recovery in the areas (Presidencia de la Nación República Argentina, 2026a; Presidencia de la Nación Argentina, 2026b). It urges the AFE to coordinate actions to prevent and combat fires, mitigate the consequences in population health, livelihoods, and belongings and support affected provinces (Presidencia de la Nación República Argentina, 2026).

4.4.4 Prevention

Wildfire risk management in Argentina and Chile is structured through consolidated institutional frameworks that have progressively evolved from a reactive fire-suppression approach toward more comprehensive, integrated risk management models. In Chile, the CONAF coordinates strategic instruments such as the Specific Emergency Plan, while in Argentina the SNMF centralizes regulatory functions and interjurisdictional assistance. Both countries rely on technical protocols, prevention guidelines, and contingency plans designed to enable early detection and rapid response (CR2, 2020; Luna et al., 2022). Mitigation measures include physical land management practices such as the construction of firebreaks, fuel reduction through brush clearing, and the manual removal of low-lying vegetation, particularly within the wildland–urban interface. Regulated use of prescribed burning is also employed to reduce fuel loads, although its implementation faces significant technical and climatic constraints (CR2, 2020).

At the household and community levels, several positive adaptation strategies have been identified, including the organization of neighborhood brigades and the maintenance of defensible space around dwellings, which contribute to strengthening social capital and local resilience (Hofflinger et al., 2025). Nevertheless, maladaptive practices persist, particularly informal settlement in high-risk areas, which significantly increases social vulnerability to wildfire disasters (Troncoso & Berwart, 2025).

Risk perception among the population plays a decisive role in shaping these behaviors. While awareness of wildfire hazards is generally high, factors such as risk habituation, economic constraints limiting vegetation management, and distrust in state-led land-use planning act as disincentives to proactive adaptation. Conversely, strong emotional attachment to place and the incorporation of local knowledge into community-based risk management have fostered more resilient responses. This evidence underscores that effective wildfire prevention requires not only technical and infrastructural measures, but also governance approaches that integrate the sociopsychological dimensions of affected communities (Walter, 2025; JRC, 2023).

4.4.5 Response - protection, containment, and extinguishment

In response to the 2026 wildfires, and difficult extinguishment conditions due to weather, the Chilean and Argentine governments have declared states of catastrophe and emergency, respectively, for the worst affected regions - Biobio and Ñuble in Chile (Ministerio del Interior, 2026), and Chubut, Rio Negro, Neuquén, La Pampa and Santa Cruz in Argentina (Sanchez, 2026).

In Chile, over 3,000 firefighters were mobilized to combat more than 75 active fires, supported by aerial operations and ground transport corridors. SENAPRED issued evacuation alerts, prompting the mass evacuation of over 50,000 residents to 11 activated shelters.

Notably, the Chilean Red Cross has developed the Red Cross Red Crescent Movement's first-ever simplified Early Action Protocol (EAP) for wildfires (Flores & Schneider, 2026; IFRC, 2025), designed to enable rapid, anticipatory interventions in high-risk scenarios. The protocol targets 2,000 people across 400 families in five municipalities. Planned early actions focus on multi-purpose cash assistance, including essential operational costs such as office and warehouse rentals, salaries for field and operations coordinators and assistants, and a lessons-learned workshop to improve future preparedness. The Ministry of Health has also provided psychosocial support to Ñuble and Biobio regions through their Mental Health Response teams (ARSAM in Spanish) (Ministry of Health Chile, 2026).

Companies across multiple sectors also provided in-kind support. Compania Cervecerias Unidas (CCU) and Soprole supplied milk, water, and essential foods for emergency kits, while SKY Airline activated air bridges (temporary air transport routes to move people, goods and supplies between locations) and logistics firms PDQ and Hualpén enabled ground transport to inaccessible areas including Penco and Lirquén (Connecting Business Initiative, 2026). In coordination with local authorities and community leaders, Desafío Levantemos Chile supported damage assessments, debris removal, and kit distribution. In parallel, the banking sector supported affected families and small- and medium enterprises (SMEs). Banco de Chile and other banks enabled emergency donations through Desafío Levantemos Chile, while BancoEstado offered nationwide relief, including loan deferrals, mobile banking in impacted areas, and assistance for customers who lost income or documents (Connecting Business Initiative, 2026).

The Regional Development Secretary announced that recovery grants will begin to be distributed, 1.5 million USD for families whose homes were completely destroyed and $750,000 for homes that were partially damaged (Ministry of Health Chile, 2026).

In Argentine Patagonia, national and provincial authorities implemented large-scale protective, containment, and suppression measures across Chubut and Rio Negro (Secretaria de Bosques, 2026). Between 8 and 12 January, over 3,000 people were evacuated from Puerto Patriada, El Hoyo, and Epuyen, including about 2,500 tourists from the Lake Puelo area, while local emergency committees in Epuyen and El Bolson activated multiple shelters providing health services and food assistance (Buenos Aires Times, 2026; Secretaria de Bosques, 2026). At the time of writing, the Government of Chubut continues to deploy extensive human and operational resources to tackle the forest fires that have broken out in various areas of the provincial mountain range. The operation involves more than 500 people, including firefighters, support and logistics personnel, and a significant number of aircraft distributed across the different affected areas (Gobierno del Chubut, 2026). In Los Alerces National Park, the Federal Emergency Management Agency alongside the National Parks Administration and the Provincial Fire Management Service, provides resources that reinforce work on the ground and enable the transfer of firefighters to areas that are difficult to access or completely inaccessible, strengthening operational capacity in highly complex scenarios (Agencia Federal de Emergencias, 2026).

At Chile's request, the EU activated its Union Protection Mechanism (UCPM), deploying a Fire Assistance Support Team (FAST) with aerial coordinators and planners (ECHO, 2026c). Following a request from Argentina, Chile, in turn, sent two aircraft to Argentine Patagonia for joint firefighting, supporting ongoing firefighting efforts across the Los Alerces National Park and other hotspots in Chubut province (Noticias Ambientales, 2026).

In the aftermath of the 2024 wildfires, Chilean local insurance markets have been directed to enhance customer support channels and ensure the rapid processing and payment of claims by the Financial Markets Commission (CMF) (FSJA, 2024). Information on Argentina's wildfire insurance is sparse, with public adjuster services like WorldClaim assisting claims but no comprehensive data exist on market exposure, claim volumes, or regulatory responses like Chile's CMF. Argentina focuses instead on firefighting support through agencies like the National Fire Management Service, leaving affected communities to rely on private insurers or public adjusters, without a centralized public program (GFDRR, 2025).

5 Summary of findings

Ongoing wildfire risk in southern Chile and Patagonia has driven increased investment in forecasting, early-action protocols, and fire response, the fires assessed here exceeded local containment capacity due to monitoring limitations, land-use practices, and highly flammable non-native pine plantations near settlements. Wildfires have caused severe ecological damage, threatening endemic species and protected areas such as Los Alerces National Park.

Our analysis, using the Hot Dry Windy Index (HDWI) to characterise weather conditions conducive to wildfires, shows that the fire-weather conditions driving these events correspond to 1-in-5-year extremes in today's climate but would have been substantially rarer in a cooler pre-industrial world, with human-induced climate change increasing their likelihood by around threefold in Chile and about 2.5-fold in northern Patagonia. The fires occurred in a season of unusually low rainfall, which was made 20-25% lower in intensity due to human-induced climate change. High temperatures, and large-scale climate variability compounded the events but the exact effect of the different modes of variability is different on different components of fire prone conditions (see sections 2.1 and 2.2) and does generally not affect the trend related to GMST. Climate models consistently project worsening fire weather and declining rainfall in both study regions, underscoring the urgent need for climate-informed land-use planning, plantation management, and risk reduction at the urban–rural interface.

Data availability

All time series used in the attribution analysis are available via the Climate Explorer.

References

All references are given as hyperlinks in the text.

Appendices

A1 Data and methods

A1.1 Observational data

We first use reanalysis data to estimate the return period of a similar event in the present day and to assess the historical trends with increasing GMST and relevant modes of variability. In this study, due to the need for multiple variables to calculate the HDWI, we used a single reanalysis product.

- **ERA5-Land** - This product is a replay of the land component of the ERA5 climate reanalysis (Muñoz-Sabater et al., 2021) produced by the European Centre for Medium-Range Weather Forecasts, with a finer spatial resolution of 0.1° (~9km grid spacing), at hourly time steps from 1950 to 5 days before the current date. The land model used is the tiled ECMWF Scheme for Surface Exchanges over Land incorporating land surface hydrology (H-TESSEL). We use daily precipitation, relative humidity, daily maximum and minimum temperature and daily maximum sustained wind speed data from this product at a resolution of 0.1°×0.1°. Due to known issues with reanalysis data in this region, we only use data from the 1979 onwards.

To characterise the large-scale drivers affecting these extremes indices, we use the following datasets as covariates:

- As a measure of anthropogenic climate change we use the 4-year rolling average (centred on the third year) global mean surface temperature (GMST), where GMST is taken from the National Aeronautics and Space Administration (NASA) Goddard Institute for Space Science (GISS) surface temperature analysis (GISTEMP, Hansen et al., 2010 and Lenssen et al. 2019).

- As a measure of the El Niño - Southern Oscillation cycle (ENSO) we use the detrended Niño3.4 index. This is computed from NOAA's ERSST v.5 sea surface temperatures, by subtracting the mean tropical SST (20°S-20°N) from the mean SST over the Nino3.4 region (5°S-5°N, 170°W-120°W). This index is therefore adjusted to remove the linear trend associated with climate change as proposed in van Oldenborgh et al., 2021, but without rescaling each calendar month.

- As a measure of the Southern Annular Mode (SAM) we use the station-based index of zonal pressure difference between the latitudes of 40°S and 65°S, based on normalised monthly sea level pressure from six stations at each of these two latitudes (Marshall, 2003; data access via https://legacy.bas.ac.uk/met/gjma/sam.html). We detrend the SAM by regressing against the smoothed GMST time series and subtracting the fitted trend, to ensure that the two time series are not confounded. The whole contribution from global warming is therefore associated with the GMST covariate, even when mediated via changes in the SAM.

The active fire information shown in Figure 1.1 is taken from NASA's Fire Information for Resource Management System (FIRMS) moderate resolution imaging spectroradiometer (MODIS MCD14DL) Collection 6. To minimise the risk of false positive detections, only fire pixels assigned a confidence above 80% are shown.

A1.2 Model and experiment descriptions

Due to the small size of the study regions, we require relatively high-resolution climate models, which restricts the number of ensembles available. We use an ensemble of regional climate models from the Coordinated Regional Climate Downscaling Experiment CORDEX-CORE multi-model ensemble (Giorgi and Gutowski, 2015; Giorgi et al., 2021), comprising eighteen simulations resulting from various pairings of Global Climate Models (GCMs) and Regional Climate Models (RCMs): six models at 0.22° resolution (SAM-22) and twelve models at 0.44° resolution (SAM-44). These simulations are composed of historical simulations up to 2005, and extended to the year 2100 using the RCP8.5 scenario.

A1.3 Statistical methods

Methods for observational and model analysis and for model evaluation and synthesis are used according to the World Weather Attribution Protocol, described in Philip et al., (2020), with supporting details found in van Oldenborgh et al., (2021), Ciavarella et al., (2021), Otto et al., (2024) and here. The key steps, presented in sections 3-6, are: (3) trend estimation from observations; (4) model validation; (5) multi-method multi-model attribution; and (6) synthesis of the attribution statement.

In this report we analyse time series of HDWI, and November-January precipitation, effective precipitation and potential evapotranspiration in regions in Chile and Patagonia. For each time series we estimate the parameters of a nonstationary statistical model in which the index depends on the GMST. In order to examine the effect of the ENSO and SAM phases on the indices alongside that of increasing GMST, we extend the nonstationary model to accommodate two additional covariates. Table A.1 summarises the time series used in this report, and the statistical distributions and assumptions used, as well as the covariates incorporated into the model in each case.

This model is then used to estimate the return period and intensity of the event under study for the 2026 GMST and for a 1.3°C cooler counterfactual climate: this allows us to compare the expected intensity and frequency of similar events now and in the preindustrial past (1850-1900, based on the Global Warming Index), by calculating the probability ratio (PR; the factor-change in the event's probability) and change in intensity of the event.

Region	**Variable**	**Distribution**	**Fit type**	**Covariates**
Chile	HDWI	GEV	Shift & scale	GMST
	NDJ Precip	lognormal	Shift	GMST & SAM
	NDJ PET	normal	Shift	GMST & ENSO

	NDJ Eff PR	normal	Shift	GMST & ENSO
Patagonia	HDWI	GEV	Shift	GMST
	NDJ Precip	lognormal	Shift	GMST & SAM
	NDJ PET	normal	Shift	GMST & ENSO
	NDJ eff PR	normal	Shift	GMST & SAM

Table A.1: *Summary of time series of indices and statistical models used to estimate the influence of different covariates in these metrics.*

In each case, the variable of interest, X, is assumed to follow a GEV/normal/lognormal distribution (Table A.1) in which the location and scale parameters vary with GMST, ENSO and SAM. For instance, the GEV distribution is given by:

$$X \sim GEV(\mu, \sigma, \xi \mid \mu_0, \sigma_0, \alpha, \beta, \eta, T, I, S),$$

where X denotes the variable of interest, HDWI; T is the smoothed GMST; I is the detrended Niño3.4 index; S is the SAM index; μ_0, σ_0 and ξ are the location, scale and shape parameters of the nonstationary distribution; and α, β and η are the trends due to GMST, ENSO and SAM, respectively. As a result, the location and scale (for shift & scale) of the distribution have a different value in each year, determined by the GMST, Niño3.4 and SAM states. The shift formulation is given by

$$\mu = \mu_0 + \alpha T + \beta I + \eta S \qquad \text{and} \qquad \sigma = \sigma_0,$$

And the shift & scale formulation is given by

$$\mu = \mu_0 + \alpha_\mu T + \beta_\mu I + \eta_\mu S \qquad \text{and} \qquad \sigma = \sigma_0 exp\left(\alpha_\sigma T + \beta_\sigma I + \eta_\sigma S\right).$$

This formulation means that the indices will shift (or shift & scale) with the strength of the detrended Niño3.4 index and the SAM index. Under this model, the effects of GMST and the other indices are assumed to be independent of one another, so that the change in intensity due to GMST is unaffected by the change in intensity due to the ENSO phase and the SAM phase. We note that this may not be the case in the real world, as, for instance, the intensity and frequency of El Niño events may have been influenced by climate change (Cai et al., 2021); however, by using detrended Niño3.4 and SAM indices (see Section 2.1) we aim to minimise the correlation between the three factors, and so do not expect the qualitative findings of this study to be affected by this simplifying assumption.

A2 Additional plots and tables for observational analysis

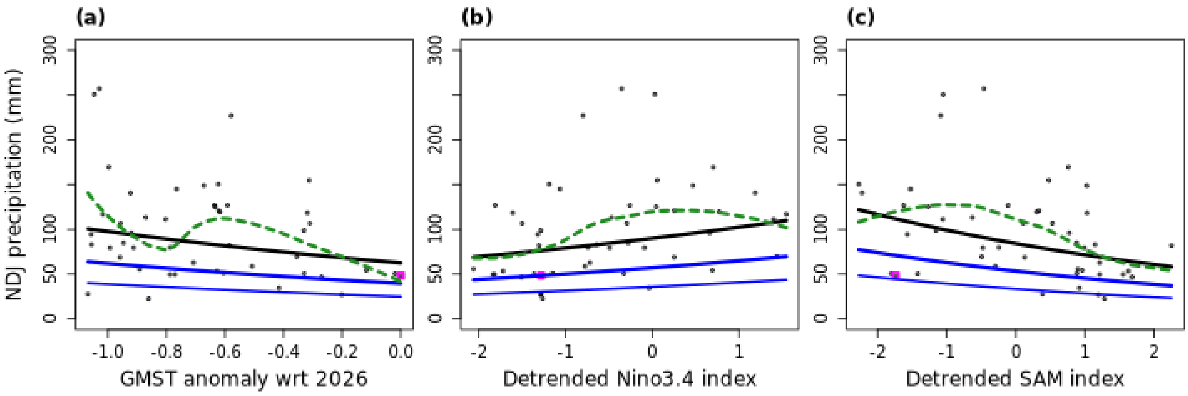

Figure A2.1: Estimated relationship between NDJ precipitation in Chile and each of the three covariates in the model: (a) GMST; (b) detrended Niño3.4 index; (c) detrended SAM index. Solid black line denotes the mean of the distribution. Blue lines indicate the expected magnitude of a 1-in-6-year (thick line) and 1-in-40-year low rainfall event (thin line). Green dashed line is a nonparametric Loess smoother. The 2025-26 observation is highlighted with a magenta box. Data: ERA5-Land.

Covariates	Probability ratio for NDJ precipitation (Chile)			Return period	AIC
	GMST	ENSO	SAM		
GMST only	7.25 (0.945, 165)	-	-	2.8 (1.65, 7.5)	72.8
GMST + ENSO	4.15 (0.48, 90.9)	1.73 (1.15, 4.07)	-	2.53 (1.47, 7.79)	69.4
GMST + SAM	23.2 (0.645, 5170)	-	0.4 (0.111, 0.657)	7.29 (2.94, 88.8)	65.2
GMST + ENSO + SAM	11.5 (0.373, 2350)	1.76 (0.925, 4.59)	0.474 (0.124, 0.77)	5.68 (2.46, 60.7)	64.5

Table A2.1: As Table 2.3, but for probability ratio (factor change in likelihood) of NDJ precipitation of the magnitude observed in 2025-2026. The model that fits the data best is shaded purple. The model used in the attribution is shaded yellow.

Covariates	% change in NDJ PET (Chile)			Return period	AIC
	GMST	ENSO	SAM		
GMST only	7.95 (3.09, 12.8)	-	-	16.1 (5.72, 125)	-29.5
GMST + ENSO	6.29 (2.06, 10.9)	2.21 (1.02, 3.48)	-	17 (5.84, 165)	-39.8
GMST + SAM	7.95 (2.44, 13.2)	-	-1.33 (-2.53, -0.29)	47.6 (9.14, 13300)	-31.4
GMST + ENSO + SAM	6.45 (1.7, 11.2)	2 (0.606, 3.43)	-0.745 (-1.97, 0.501)	32.7 (6.99, 4890)	-39.2

Table A2.2: As Table 2.3, but for change in intensity of NDJ potential evapotranspiration. The model that fits the data best is shaded purple.

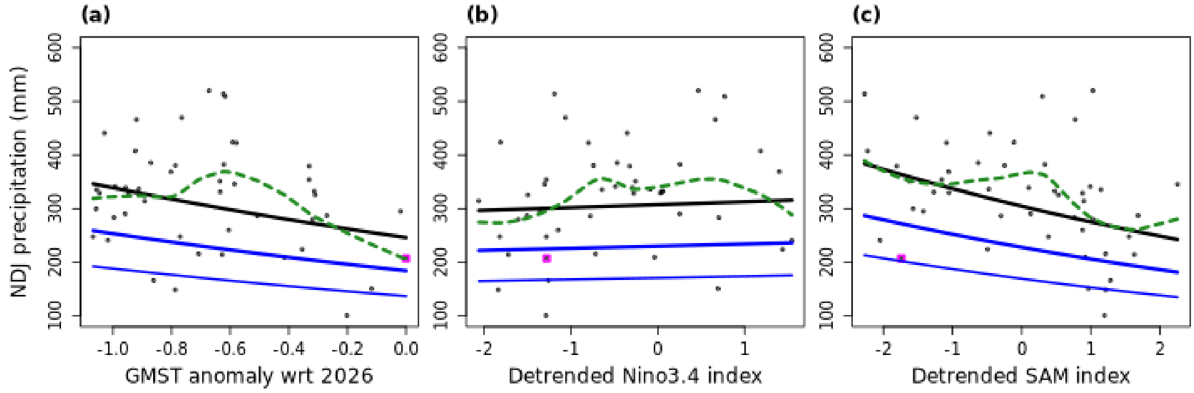

Figure A2.2: Estimated relationship between NDJ precipitation in the Patagonian study region and each of the three covariates in the model: (a) GMST; (b) detrended Niño3.4 index; (c) detrended SAM index. Solid black line denotes the mean of the distribution. Blue lines indicate the expected magnitude of a 1-in-6-year (thick line) and 1-in-40-year low rainfall event (thin line). Green dashed line is a nonparametric Loess smoother. The 2025-26 observation is highlighted with a magenta box. Data: ERA5-Land.

Covariates	Probability ratio for NDJ precipitation (Patagonia)			Return period	AIC
	GMST	ENSO	SAM		
GMST only	9.08 (1.22, 104)	-	-	3.26 (1.65, 15.2)	147
GMST + ENSO	6.55 (0.575, 110)	1.3 (0.777, 3.72)	-	3.09 (1.55, 18.5)	147
GMST + SAM	25.9 (1.32, 2450)	-	0.422 (0.107, 0.767)	8.12 (3.01, 124)	141
GMST + ENSO + SAM	21.5 (0.612, 5700)	1.13 (0.434, 4.18)	0.442 (0.0985, 0.823)	7.61 (2.77, 132)	143

Table A2.3: As Table 2.7, but for probability ratio (factor change in likelihood) of NDJ precipitation of the magnitude observed in 2025-2026 in the Patagonia study region. The model that fits the data best is shaded purple. The model used in the attribution is shaded yellow.

Covariates	% change in NDJ PET (Patagonia)			Return period	AIC
	GMST	ENSO	SAM		
GMST only	*8.21 (1.97, 15.1)*	-	-	*8.99 (4.15, 43.5)*	*-6.91*
GMST + ENSO	*6.37 (0.056, 13.1)*	*2.45 (0.444, 5.03)*	-	*8.29 (3.77, 40.6)*	*-10.4*
GMST + SAM	*8.21 (1.14, 15.4)*	-	*-2.34 (-4.35, -0.227)*	*25.6 (7.32, 985)*	*-9.73*

GMST + ENSO + SAM	*6.74 (0.33, 14.4)*	*1.94 (-0.36, 4.72)*	*-1.78 (-4.02, 0.352)*	*18.5 (5.87, 603)*	*-11.1*

Table A2.4: As Table 2.7, but for change in intensity of NDJ potential evapotranspiration. The model that fits the data best is shaded purple.

A3 Model evaluation tables

Model / Observations	Seasonal	Spatial	Shape parameter	Overall	Keep?
ERA5-Land			0.0268 (-0.283, 0.292)		
CORDEX			0.0814 (-0.304, 2.07)		
SAM-22_HadGEM2-ES_r1i1p1 RegCM4-7	good	good	-0.0502 (-0.529, 0.237)	good	Y
SAM-22_HadGEM2-ES_r1i1p1 REMO2015	good	good	0.0381 (-0.213, 0.268)	good	Y
SAM-22_MPI-ESM-LR_r1i1p1 REMO2015	good	good	-0.165 (-0.509, 0.135)	good	Y
SAM-22_MPI-ESM-MR_r1i1p1 RegCM4-7	good	good	-0.163 (-0.417, 0.0462)	good	Y
SAM-22_NorESM1-M_r1i1p1 RegCM4-7	reasonable	good	-0.0763 (-0.328, 0.144)	reasonable	N
SAM-22_NorESM1-M_r1i1p1 REMO2015	good	good	-0.11 (-0.411, 0.191)	good	Y
SAM-44_CanESM2_r1i1p1 RCA4	good	good	-0.0674 (-0.306, 0.244)	good	Y
SAM-44_CNRM-CM5_r1i1p1 RCA4	good	good	-0.359 (-0.722, -0.0933)	reasonable	N
SAM-44_CSIRO-Mk3-6-0_r1i1p1 RCA4	good	good	-0.224 (-0.399, -0.00438)	good	Y
SAM-44_EC-EARTH_r12i1p1 RCA4	good	good	-0.236 (-0.542, 0.0752)	good	Y
SAM-44_GFDL-ESM2M_r1i1p1 RCA4	reasonable	good	-0.12 (-0.483, 0.11)	reasonable	N
SAM-44_HadGEM2-ES_r1i1p1 RCA4	reasonable	good	0.184 (-0.107, 0.561)	reasonable	N
SAM-44_IPSL-CM5A-MR_r1i1p1 RCA4	good	good	-0.196 (-0.563, 0.241)	good	Y

SAM-44_MIROC5_r1i1p1 RCA4	reasonable	good	-0.0426 (-0.282, 0.191)	reasonable	N
SAM-44_MPI-ESM-LR_r1i1p1 RCA4	reasonable	good	0.0504 (-0.217, 0.386)	reasonable	N
SAM-44_NorESM1-M_r1i1p1 RCA4	reasonable	good	-0.146 (-0.566, 0.109)	reasonable	N

Table A3.1: Evaluation results of the climate models considered for attribution analysis of HDWI2x in Chile. The evaluation of the seasonal cycle and spatial pattern are shown, along with the estimated shape parameters, including 95% confidence intervals. The final evaluation is based on all three criteria. The scale parameter is not used in this evaluation because it is a nonstationary parameter in this case.

Model / Observations	**Seasonal**	**Spatial**	**Scale parameter**	**Overall**	**Keep**
ERA5-Land			0.538 (0.42, 0.636)		
CORDEX					
SAM-22_HadGEM2-ES_r1i1p1 RegCM4-7	reasonable	good	0.591 (0.466, 0.686)	reasonable	Y
SAM-22_HadGEM2-ES_r1i1p1 REMO2015	good	good	0.434 (0.351, 0.494)	good	Y
SAM-22_MPI-ESM-LR_r1i1p1 REMO2015	reasonable	good	0.368 (0.282, 0.43)	reasonable	Y
SAM-22_MPI-ESM-MR_r1i1p1 RegCM4-7	reasonable	good	0.541 (0.425, 0.642)	reasonable	Y
SAM-22_NorESM1-M_r1i1p1 RegCM4-7	good	good	0.748 (0.614, 0.839)	reasonable	Y
SAM-22_NorESM1-M_r1i1p1 REMO2015	good	good	0.468 (0.376, 0.531)	good	Y
SAM-44_CanESM2_r1i1p1 RCA4	reasonable	bad	0.524 (0.398, 0.619)	bad	N
SAM-44_CNRM-CM5_r1i1p1 RCA4	bad	bad	0.339 (0.27, 0.386)	bad	N
SAM-44_CSIRO-Mk3-6-0_r1i1p1 RCA4	reasonable	bad	0.438 (0.353, 0.5)	bad	N
SAM-44_EC-EARTH_r12i1p1 RCA4	good	bad	0.406 (0.312, 0.469)	bad	N
SAM-44_GFDL-ESM2M_r1i1p1 RCA4	bad	bad	0.399 (0.322, 0.454)	bad	N
SAM-44_HadGEM2-ES_r1i1p1 RCA4	reasonable	bad	0.448 (0.364, 0.509)	bad	N

SAM-44_HadGEM2-ES_r1i1p1 RegCM4-3	reasonable	reasonable	0.454 (0.36, 0.53)	reasonable	Y
SAM-44_IPSL-CM5A-MR_r1i1p1 RCA4	reasonable	bad	0.537 (0.398, 0.644)	bad	N
SAM-44_MIROC5_r1i1p1 RCA4	reasonable	bad	0.4 (0.298, 0.478)	bad	N
SAM-44_MPI-ESM-LR_r1i1p1 RCA4	reasonable	bad	0.39 (0.308, 0.452)	bad	N
SAM-44_MPI-ESM-LR_r1i1p1 REMO2009	reasonable	good	0.383 (0.307, 0.439)	reasonable	Y
SAM-44_NorESM1-M_r1i1p1 RCA4	reasonable	bad	0.483 (0.386, 0.561)	bad	N

Table A3.2: Evaluation results of the climate models considered for attribution analysis of pr-NDJ in Chile. The evaluation of the seasonal cycle and spatial pattern are shown, along with the estimated scale parameters, including 95% confidence intervals. The final evaluation is based on all three criteria. The scale parameter is not used in this evaluation because it is a nonstationary parameter in this case.

Model / Observations	**Seasonal**	**Spatial**	**Scale parameter**	**Shape parameter**	**Overall**	**Keep**
ERA5-Land			0.654 (0.486, 0.799)	-0.127 (-0.408, 0.152)		
CORDEX						
SAM-22_HadGEM2-ES_r1i1p1 RegCM4-7	good	good	0.758 (0.519, 0.945)	0.011 (-0.323, 0.337)	good	Y
SAM-22_HadGEM2-ES_r1i1p1 REMO2015	good	good	0.601 (0.422, 0.741)	-0.0251 (-0.441, 0.41)	good	Y
SAM-22_MPI-ESM-LR_r1i1p1 REMO2015	good	good	0.508 (0.385, 0.62)	-0.00495 (-0.199, 0.218)	good	Y
SAM-22_MPI-ESM-MR_r1i1p1 RegCM4-7	good	good	0.943 (0.709, 1.13)	-0.379 (-0.735, -0.0105)	reasonable	Y
SAM-22_NorESM1-M_r1i1p1 RegCM4-7	good	good	0.581 (0.419, 0.708)	-0.0402 (-0.294, 0.237)	good	Y
SAM-22_NorESM1-M_r1i1p1 REMO2015	good	good	0.367 (0.265, 0.448)	0.0021 (-0.311, 0.372)	bad	N
SAM-44_CanESM2_r1i1p1 RCA4	good	good	0.42 (0.309, 0.542)	0.154 (-0.154, 0.423)	reasonable	Y
SAM-44_CNRM-CM5_r1i1p1 RCA4	good	good	0.368 (0.261, 0.478)	0.323 (0.0513, 0.716)	bad	N
SAM-44_CSIRO-Mk3-6-0_r1i1p1 RCA4	good	good	0.614 (0.437, 0.744)	0.0857 (-0.134, 0.408)	good	Y
SAM-44_EC-EARTH_r12i1p1 RCA4	good	good	0.377 (0.259, 0.533)	0.272 (-0.118, 0.674)	reasonable	Y

SAM-44_GFDL-ESM2M_r1i1p1 RCA4	reasonable	good	0.476 (0.367, 0.59)	0.0245 (-0.187, 0.211)	reasonable	Y
SAM-44_HadGEM2-ES_r1i1p1 RCA4	good	good	0.564 (0.384, 0.845)	0.159 (-0.506, 0.586)	reasonable	Y
SAM-44_IPSL-CM5A-MR_r1i1p1 RCA4	good	good	0.558 (0.409, 0.698)	0.223 (0.0141, 0.588)	reasonable	Y
SAM-44_MIROC5_r1i1p1 RCA4	good	good	0.337 (0.226, 0.452)	0.33 (-0.0118, 0.662)	bad	N
SAM-44_MPI-ESM-LR_r1i1p1 RCA4	good	good	0.391 (0.256, 0.551)	0.434 (0.137, 0.879)	reasonable	Y
SAM-44_NorESM1-M_r1i1p1 RCA4	good	good	0.384 (0.267, 0.471)	0.146 (-0.173, 0.548)	bad	N

Table A3.3: Evaluation results of the climate models considered for attribution analysis of HDWI5x in Patagonia. The evaluation of the seasonal cycle and spatial pattern are shown, along with the estimated shape parameters, including 95% confidence intervals. The final evaluation is based on all four criteria. The scale parameter is not used in this evaluation because it is a nonstationary parameter in this case.

Model / Observations	**Seasonal**	**Spatial**	**Scale parameter**	**Overall**	**Keep**
ERA5-Land			0.326 (0.244, 0.395)		
CORDEX					
SAM-22_HadGEM2-ES_r1i1p1 RegCM4-7	reasonable	good	0.299 (0.237, 0.346)	reasonable	Y
SAM-22_HadGEM2-ES_r1i1p1 REMO2015	reasonable	good	0.299 (0.245, 0.336)	reasonable	Y
SAM-22_MPI-ESM-LR_r1i1p1 REMO2015	bad	good	0.272 (0.213, 0.318)	bad	N
SAM-22_MPI-ESM-MR_r1i1p1 RegCM4-7	bad	good	0.257 (0.203, 0.292)	bad	N
SAM-22_NorESM1-M_r1i1p1 RegCM4-7	reasonable	good	0.223 (0.17, 0.264)	reasonable	Y
SAM-22_NorESM1-M_r1i1p1 REMO2015	reasonable	good	0.221 (0.174, 0.255)	reasonable	Y
SAM-44_CanESM2_r1i1p1 RCA4	reasonable	bad	0.258 (0.205, 0.301)	bad	N
SAM-44_CNRM-CM5_r1i1p1 RCA4	reasonable	bad	0.192 (0.151, 0.223)	bad	N
SAM-44_CSIRO-Mk3-6-0_r1i1p1 RCA4	bad	bad	0.21 (0.163, 0.247)	bad	N

SAM-44_EC-EARTH_r12i1p1 RCA4	bad	bad	0.247 (0.178, 0.294)	bad	N
SAM-44_GFDL-ESM2M_r1i1p1 RCA4	bad	bad	0.191 (0.154, 0.22)	bad	N
SAM-44_HadGEM2-ES_r1i1p1 RCA4	good	bad	0.272 (0.22, 0.311)	bad	N
SAM-44_HadGEM2-ES_r1i1p1 RegCM4-3	good	reasonable	0.311 (0.249, 0.357)	reasonable	Y
SAM-44_IPSL-CM5A-MR_r1i1p1 RCA4	reasonable	bad	0.268 (0.21, 0.309)	bad	N
SAM-44_MIROC5_r1i1p1 RCA4	reasonable	bad	0.189 (0.149, 0.219)	bad	N
SAM-44_MPI-ESM-LR_r1i1p1 RCA4	bad	bad	0.263 (0.207, 0.302)	bad	N
SAM-44_MPI-ESM-LR_r1i1p1 REMO2009	bad	good	0.265 (0.213, 0.307)	bad	N
SAM-44_NorESM1-M_r1i1p1 RCA4	reasonable	bad	0.179 (0.139, 0.209)	bad	N

Table A3.4: Evaluation results of the climate models considered for attribution analysis of pr-NDJ in Patagonia. The evaluation of the seasonal cycle and spatial pattern are shown, along with the estimated scale parameters, including 95% confidence intervals. The final evaluation is based on all three criteria. The scale parameter is not used in this evaluation because it is a nonstationary parameter in this case.

A4 Estimated trends in climate models

Table A.4.1: *Changes in intensity and probability ratios for what was in 2026 a 1-in-5-year HDWI2x event over the Chile study region, for observational datasets and for each model that passed evaluation: 'past warming': from the 1.3°C cooler preindustrial climate to the present; 'future warming': from the present to 2.6°C above preindustrial (1.3°C warmer than the present). All results are presented to 3 significant figures.*

	Change in intensity (kPa m/s)		**Probability ratio**	
Dataset **Obs / models**	**Past warming**	**Future warming**	**Past warming**	**Future warming**
ERA5-Land	6.39 (2.17, 8.13)		198 (2.53, Inf)	
SAM-22_HadGEM2-ES_r1i1p1 RegCM4-7	-0.561 (-2.41, 1.66)	0.692 (0.0844, 1.27)	0.749 (0.347, 6.31)	1.42 (1.06, 1.84)
SAM-22_HadGEM2-ES_r1i1p1 REMO2015	3.77 (0.238, 10.1)	2.82 (1.86, 3.87)	3.47 (1.06, 67.1)	2.11 (1.72, 2.69)
SAM-22_MPI-ESM-LR_r1i1p1 REMO2015	2.94 (-0.429, 5.94)	2.64 (0.642, 4.74)	6.09 (0.839, Inf)	1.84 (1.24, 2.37)

SAM-22_MPI-ESM-MR_r1i1p1 RegCM4-7	1.72 (-0.983, 4.51)	1.77 (0.716, 2.97)	2.31 (0.729, 369)	1.92 (1.39, 2.64)
SAM-22_NorESM1-M_r1i1p1 REMO2015	4.98 (-0.447, 10.6)	2.53 (0.647, 4.52)	5.53 (0.908, Inf)	1.99 (1.31, 2.71)
SAM-44_CanESM2_r1i1p1 RCA4	3.12 (0.992, 5.46)	3.06 (2.22, 4.06)	5.56 (1.69, 50.7)	2.58 (2.25, 3.05)
SAM-44_CSIRO-Mk3-6-0_r1i1p1 RCA4	0.807 (-2.44, 3.55)	1.28 (0.301, 2.24)	1.43 (0.453, 11)	1.75 (1.19, 2.39)
SAM-44_EC-EARTH_r12i1p1 RCA4	3.65 (0.721, 6.75)	2.68 (1.48, 3.83)	10.8 (1.39, Inf)	2.2 (1.72, 2.72)
SAM-44_IPSL-CM5A-MR_r1i1p1 RCA4	1.5 (-0.544, 3.89)	2.04 (1.14, 2.99)	2.12 (0.79, 15.6)	1.96 (1.59, 2.41)

Table A.4.2: *Changes in intensity and probability ratios for what was in 2026 a 1-in-5-year November-January precipitation event over the Chile study region, for observational datasets and for each model that passed evaluation: 'past warming': from the 1.3°C cooler preindustrial climate to the present; 'future warming': from the present to 2.6°C above preindustrial (1.3°C warmer than the present). All results are presented to 3 significant figures.*

Dataset **Obs / models**	**Change in intensity (%)**		**Probability ratio**	
	Past warming	**Future warming**	**Past warming**	**Future warming**
ERA5-Land	-50 (-74.2, 2.14)		7.25 (0.945, 165)	
SAM-22_HadGEM2-ES_r1i1p1 RegCM4-7	-30 (-52.5, 3.64)	-32.1 (-51.9, -16.5)	2.69 (0.929, 15)	1.64 (1.33, 2.01)
SAM-22_HadGEM2-ES_r1i1p1 REMO2015	-19.4 (-40.1, 5.62)	-34.7(-47.4, -24)	2.31 (0.836, 12.8)	2.17 (1.79, 2.65)
SAM-22_MPI-ESM-LR_r1i1p1 REMO2015	-15.1 (-36.1, 12.9)	-35.7 (-53.5, -18)	2.02 (0.645, 11)	2.29 (1.65, 3.01)
SAM-22_MPI-ESM-MR_r1i1p1 RegCM4-7	16 (-30.5, 99.3)	-20.9 (-45.8, -3.47)	0.719 (0.309, 2.94)	1.53 (1.09, 2.15)
SAM-22_NorESM1-M_r1i1p1 RegCM4-7	-19 (-66.9, 62.9)	-21.2 (-50.9, 1.63)	1.51 (0.455, 21.2)	1.39 (0.97, 1.9)
SAM-22_NorESM1-M_r1i1p1 REMO2015	-24.2 (-56.3, 23.4)	-23 (-40.9, -8.44)	2.56 (0.561, 42.3)	1.71 (1.26, 2.31)
SAM-44_HadGEM2-ES_r1i1p1 RegCM4-3	-8.31 (-37.6, 29.9)	-10.1 (-21.7, -0.497)	1.32 (0.489, 7)	1.32 (1.02, 1.71)
SAM-44_MPI-ESM-LR_r1i1p1 REMO2009	-12.6 (-31.6, 9.95)	-35.2 (-52.6, -19.1)	1.69 (0.715, 5.43)	2.2 (1.64, 2.81)

Table A.4.3: *Changes in intensity and probability ratios for what was in 2026 a 1-in-5-year HDWI2x event over the Patagonia study region, for observational datasets and for each model that passed evaluation: 'past warming': from the 1.3°C cooler preindustrial climate to the present; 'future warming': from the present to 2.6°C above preindustrial (1.3°C warmer than the present). All results are presented to 3 significant figures.*

Dataset **Obs / models**	**Change in intensity (kPa m/s)**		**Probability ratio**	
	Past warming	**Future warming**	**Past warming**	**Future warming**
ERA5-Land	1.78 (0.947, 2.5)		24 (4.77, Inf)	
SAM-22_HadGEM2-ES_r1i1p1 RegCM4-7	0.863 (0.34, 1.47)	0.591 (0.391, 0.895)	2.77 (1.48, 9.95)	1.69 (1.39, 2.26)
SAM-22_HadGEM2-ES_r1i1p1 REMO2015	0.515 (-0.0284, 0.888)	0.376 (0.247, 0.527)	2.07 (0.957, 4.02)	1.67 (1.4, 2.11)
SAM-22_MPI-ESM-LR_r1i1p1 REMO2015	0.858 (0.466, 1.24)	0.523 (0.327, 0.733)	6.62 (2.29, 41.8)	2.18 (1.63, 2.96)
SAM-22_MPI-ESM-MR_r1i1p1 RegCM4-7	1.28 (0.462, 2.19)	0.991 (0.669, 1.39)	20 (2.2, Inf)	2.32 (1.78, 3.31)
SAM-22_NorESM1-M_r1i1p1 RegCM4-7	0.525 (-0.158, 1.2)	0.66 (0.363, 0.965)	2.7 (0.775, 31.6)	2.26 (1.58, 3.13)
SAM-44_CanESM2_r1i1p1 RCA4	0.51 (0.325, 0.731)	0.682 (0.477, 0.894)	2.58 (1.75, 4.94)	2.43 (1.79, 3.29)
SAM-44_CSIRO-Mk3-6-0_r1i1p1 RCA4	0.13 (-0.463, 0.923)	0.321 (0.186, 0.524)	1.19 (0.58, 3.91)	1.45 (1.22, 1.95)
SAM-44_EC-EARTH_r12i1p1 RCA4	0.325 (0.127, 0.57)	0.32 (0.211, 0.52)	1.68 (1.23, 2.83)	1.56 (1.3, 2.18)
SAM-44_GFDL-ESM2M_r1i1p1 RCA4	0.462 (0.0729, 0.852)	0.295 (0.183, 0.421)	1.98 (1.12, 5.56)	1.45 (1.25, 1.74)
SAM-44_HadGEM2-ES_r1i1p1 RCA4	0.833 (0.566, 1.14)	0.379 (0.264, 0.524)	2.97 (1.83, 6.37)	1.51 (1.29, 1.89)
SAM-44_IPSL-CM5A-MR_r1i1p1 RCA4	0.396 (0.161, 0.693)	0.551 (0.43, 0.741)	1.64 (1.21, 2.56)	1.75 (1.48, 2.3)
SAM-44_MPI-ESM-LR_r1i1p1 RCA4	0.363 (0.224, 0.549)	0.257 (0.112, 0.433)	1.7 (1.36, 2.58)	1.41 (1.14, 1.94)

Table A.4.4: *Changes in intensity and probability ratios for what was in 2026 a 1-in-5-year November-January precipitation event over the Patagonia study region, for observational datasets and for each model that passed evaluation: 'past warming': from the 1.3°C cooler preindustrial climate to the present; 'future warming': from the present to 2.6°C above preindustrial (1.3°C warmer than the present). All results are presented to 3 significant figures.*

Dataset **Obs / models**	**Change in intensity (%)**		**Probability ratio**	
	Past	**Future**	**Past**	**Future**

	warming	warming	warming	warming
ERA5-Land	-35 (-58.5, -3.46)		9.08 (1.22, 104)	
SAM-22_HadGEM2-ES_r1i1p1 RegCM4-7	-15.3 (-31.1, 3.01)	-8.8 (-16.2, -1.46)	2.6 (0.863, 17.3)	1.45 (1.07, 1.93)
SAM-22_HadGEM2-ES_r1i1p1 REMO2015	-14.6 (-30, 3.18)	-11.5 (-19, -4.25)	2.49 (0.853, 14.6)	1.64 (1.22, 2.17)
SAM-22_NorESM1-M_r1i1p1 RegCM4-7	-6.36 (-27.3, 17.6)	-15.4 (-26, -5.09)	1.53 (0.44, 18.1)	1.92 (1.29, 2.68)
SAM-22_NorESM1-M_r1i1p1 REMO2015	-8.62 (-31.3, 16.6)	-16 (-27, -5.73)	1.79 (0.449, 20.4)	1.96 (1.34, 2.75)
SAM-44_HadGEM2-ES_r1i1p1 RegCM4-3	-8.72 (-28, 14.6)	-3.47 (-11.6, 3.44)	1.56 (0.576, 8.32)	1.17 (0.841, 1.64)